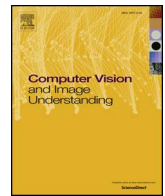




Contents lists available at ScienceDirect

Computer Vision and Image Understanding

journal homepage: www.elsevier.com/locate/cviu

A geometric approach for color image regularization

Freddie Åström^{*,a}, Christoph Schnörr^b^a Heidelberg Collaboratory for Image Processing, Heidelberg University, Heidelberg, Germany^b Image and Pattern Analysis Group, Heidelberg University, Heidelberg, Germany

ARTICLE INFO

Keywords:

Image analysis
 Color image restoration
 Vectorial total variation
 Double-opponent space
 Split-Bregman
 Non-convex regularization

ABSTRACT

We present a new vectorial total variation method that addresses the problem of color consistent image filtering. Our approach is inspired from the double-opponent cell representation in the human visual cortex. Existing methods of vectorial total variation regularizers have insufficient (or no) coupling between the color channels and thus may introduce color artifacts. We address this problem by introducing a novel coupling between the color channels related to a pullback-metric from the opponent space to the data (RGB color) space. Our energy is a non-convex, non-smooth higher-order vectorial total variation approach and promotes color consistent image filtering via a coupling term. For a convex variant, we show well-posedness and existence of a solution in the space of vectorial bounded variation. For the higher-order scheme we employ a half-quadratic strategy, which model the non-convex energy terms as the infimum of a sequence of quadratic functions. In experiments, we elaborate on traditional image restoration applications of inpainting, deblurring and denoising. Regarding the latter, we consider two noise scenarios i) intensity and chromaticity (the color representation of the double-opponent space) are corrupted by uniform noise and ii) only the chromaticity is corrupted with noise. In the latter case, we demonstrate state of the art restoration quality with respect to structure coherence and color consistency.

1. Introduction

1.1. Motivation

Image filtering is a fundamental operation in image processing applications. Typically image filtering refers to all type of algorithms that modify image pixels in a linear or non-linear manner. Common applications are image denoising (or smoothing) (Åström et al., 2012; Bredies et al., 2010; Iijima, 1959; Koenderink, 1984; Perona et al., 1990; Roth and Black, 2005; Tomasi and Manduchi, 1998), active contours (Kass et al., 1988), image deblurring (Chan and Wong, 1998; Oliveira et al., 2009), inpainting (Ballester et al., 2001; Chan et al., 2002) and optical flow (Horn and Schunck, 1981). These applications have in common that they can be formulated as variational problems and are thus inherently related.

In a *discrete setting*, the solution of such functionals (or energies), can be formulated as maximum a-posteriori (MAP) problems based on markov random fields (MRF), we refer to Wang et al. (2013) and Kappes et al. (2015) for such approaches. However, the size of the required label space makes the optimization problem intractable as there is one label for each possible state. Due to this drawback, one computes approximate solutions, e.g., by applying relaxation techniques of the

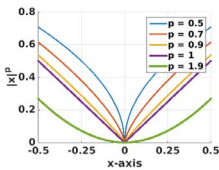
label space. The advantage of structured energy minimization, such as the MRFs formulation, is that complex neighborhoods, non-smooth and non-convex penalty functions are easily modelled.

On the other hand, *continuous models* do not suffer from large label spaces, see for example the recently introduced assignment filter (Åström et al., 2017). However, the corresponding optimization problem needs to explicitly cope with non-smoothness and non-convexity. Convex optimization techniques are well established methods that efficiently find optimal solutions of convex functions. During the past years, the imaging community has seen a surge of non-convex and often non-smooth energies, often demonstrating improved results over convex counterparts. The optimization of non-convex functions is particularly challenging since straightforward approaches often leads to locally optimal solution only.

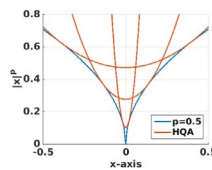
Relaxation of the non-smooth problems often include modification of the objective function and approximating non-convex penalty terms via auxiliary variables. Cohen proposed fitting of auxiliary variables (Cohen, 1996). However, this approach relies on conjugate functions and if no closed form-solutions are available the relaxation method is inefficient. Another popular approach in image processing is the half-quadratic algorithm (HQA) studied by Geman and Yang (1995). The HQA approximates a non-convex function as the infimum of quadratic

* Corresponding author.

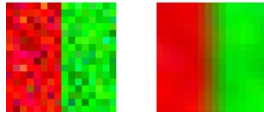
E-mail address: freddie.astroem@iwr.uni-heidelberg.de (F. Åström).<http://dx.doi.org/10.1016/j.cviu.2017.10.013>Received 29 July 2016; Received in revised form 12 October 2017; Accepted 25 October 2017
1077-3142/ © 2017 Elsevier Inc. All rights reserved.



(a) Example of different values of the p -norm for $p \in (0, 2)$.



(b) The non-convex energy realized as the infimum of quadratic functions (here $p = 0.5$).



(c) Introduction of artificial colors are shown by the smooth transition from red to green in the right panel. These types of artifacts often arise in image smoothing due to insufficient color channel coupling and the denoising scheme's lack of adaptivity to the image structure.



(d) Example of color shimmering artifacts (right) which often appear in homogeneous image regions. Color shimmering can often be suppressed with stronger smoothing, however, frequently at the cost of oversmoothing image features (corners/lines etc).

functions as illustrated in Fig. 1 (a), (b). One may also consider lagged fix-point formulations (Chan and Mulet, 1999). In this case regularity is imposed via mollification that yields a differentiable energy. Subsequently one needs to prove that there exists a convergent fixed-point algorithm.

This work builds on the convex total variation (TV) presented in the seminal work of Rudin et al. (1992). The success story of total variation (TV) began in 1992 when Rudin et al. (1992) introduced an extension of Rudin's PhD thesis (Rudin, 1987). In Rudin's work it was conjectured that the ℓ_1 norm is more appropriate as a regularizer for image processing applications than, e.g., ℓ_2 norm. The popularity of TV is mainly due to its discontinuity preserving properties, i.e., the norm is a strong prior for avoiding mode mixing and can be interpreted as the solution of a MAP problem. The common goal for noise reduction methods is to preserve characteristic image features, thus TV is a suitable prior as it is edge preserving. Features of interest vary depending on application area. However, in general one wishes to preserve structures defining dominant orientations and discontinuity points, such as edge and corners, since much of the visual information is contained in contour and differences of contrast (Ratliff, 1971). Extensions of the initial grayscale TV prior for image enhancement to color images faces the problem to characterize notions of *color*. The problem of consistent color image processing is largely unsolved and still no consensus on suitable characterization of a "color edge", or a "color boundary" for general imaging problems has been reached.

This work studies the problem of color image regularization. Extending the scalar TV to color images is a non-trivial problem. For example, if a color edge is insufficiently preserved in the smoothing process, artificial colors may emerge at the smooth transition between these colors as demonstrated by Fig. 1 (c). The same figure (d) illustrates the problem of color shimmering, i.e., insufficient smoothing of homogeneous regions. To address these problems we examine a color space representation, commonly used in computer vision applications and derive a novel color mixing term that penalizes inter-channel discontinuities. We investigate a special instance of color space representation known as the *double-opponent color space*. The key aspect of our framework builds on the observation that the Jacobian carries vital information useful for color boundary detection. Utilizing this information, we design a TV-based regularizer that describes the color information in a subspace defined by the hue and saturation of the original image color space. Via a higher-order non-convex, non-smooth energy formulation we show improved discontinuity preserving properties over convex counter-parts with respect to color consistency and structural coherence. This work extends our early work (Åström, 2016) with a geometric viewpoint, higher-order differentials, rigorous proofs and a thorough experimental evaluation. We remark further that the

Fig. 1. Figure (a) shows several instances of the non-convex ℓ_p -norm for different p values and (b) shows example HQA approximation for $p = 0.5$. Figures (c) and (d) illustrates common color image denoising artifacts.

presented work is a significant extension of Åström and Schnörr (2016) which merely introduce a first order convex scheme.

Our approach is motivated based on results from color perception:

- The connection between experienced visual stimuli and current color space models of the visual cortex is naturally modeled using tools from differential geometry. Accordingly, we adopt a geometric viewpoint to explore the relation between color edges and the regularizer based on the color space geometries. The double-opponent color space is thought to relate neurophysiological properties of color experience to single-opponent and double-opponent cells in the human cortex, see Ebner (2007); Gao et al. (2013); Land (1983; 1986) and references therein. There is recent evidence that a large concentration of double-opponent cells are located in the region V1, the primary part of the visual cortex (Conway et al., 2010). Double-opponent cells are thought to be orientation-selective with respect to color discrimination and the detection of color boundaries, results made possible by modern functional magnetic resonance imaging (fMRI) techniques (Conway et al., 2010). We will use this fact in our subsequent analysis to motivate the introduction of our model.

When formulating image denoising objective functions one often adopts different viewpoints. The following two major viewpoints motivate our work: namely color perception and color model.

- *Color perception*. As stated, we formulate the problem of color image denoising from principles of color perception. The discriminate power of color is one primary feature for object separation and detection. It is often referred to as a highly important features for the visual system and is closely related to the problem of accurate boundary detection (Conway et al., 2010). We present a model that preserves discontinuities in the color space motivated by a double-opponent transformation. By preserving color discontinuities we hypothesize that color borders trigger the activation of these double-opponent cells and thus yields the experience of crisp color borders in the image.
- *Color model*. We denote transportation of the visual (RGB) stimuli to the double-opponent cells in the visual cortex with a mapping. We postulate that, if there exists a spatial relation between two stimuli (e.g., a color difference), then this induces a response in the double-opponent cells in the form of orientation sensitivity. The motivation is that double-opponent cells act as color edge detectors, as shown by neurophysical experiments (again we refer to Ebner (2007); Gao et al. (2013); Land (1983; 1986)). Thus, we conclude that there exist a color transition function (or gradient) in the double-opponent space. To obtain the mapping we observe that the stimuli in the

opponent space, induced by a linear opponent transformation, in fact gives rise to a pullback metric on the RGB-space where the spatial interaction between the double-opponent cells are modeled by the gradient-operator.

1.2. Organization

In [Section 2](#) we sketch the framework of total variation and make the difference between our view-point to established literature in the field. Already here, we must emphasize that much research in color image processing is merely a multi-dimensional extension of the original total variation for gray-scale images. The differences between our approach and related VTV methods are also detailed in [Section 2](#). In [Section 3](#) we review color space models often adopted in the image processing literature. In the same section we also introduce the double-opponent transformation. [Section 4](#) serves to derive the connection between the observation (RGB) space and the double-opponent representation, we also derive results on the encoded information in the metric decomposition and relate these facts to *colorfulness*. The general variational problem is defined in [Section 5](#). In the same section we formulate the corresponding HQA formulation and prove that the HQA is a particular instance of a majorize-minimize algorithm for the general problem. For the particular instance corresponding to the non-relaxed, first order VTV with a convex data term, we rigorously show convexity of the overall problem, that a solution exists and is unique in [Section 5.3](#). [Section 6](#) describes the numerical scheme and [Section 7](#) presents the numerical evaluation with applications in image denoising, inpainting and deblurring. [Section 8](#) concludes the paper.

Next we review total variation methods and present current generalizations to color image processing before we introduce our framework.

2. Further related work

In addition to TV, closest to our work is the seminal work of [Sapiro and Ringach \(1996\)](#) who first observed that the metric tensor eigendecomposition can be used to describe directional change and magnitude of color images. In this work we extend this reasoning and show that there exists a natural color space representation which leads to a corresponding interpretation of the Sapiro and Ringach approach. Unlike the Beltrami flow ([Kimmel et al., 2000](#)) and ([Sapiro and Ringach, 1996](#)), we exploit the inverse rate of change of the metric tensor's eigenvalues. This gives us a transformation from the double-opponent space back to the observation space of the image data. We thus obtain an explicit information about the image chromaticity, and by extension, the color edge information. The detection of edges is a well investigated field of study for gray-scale images and methods include, e.g., the canny edge detector ([Canny, 1986](#)), gradient filters and the structure tensor ([Bigun and Granlund, 1987](#); [Förstner and Gülch, 1987](#)). These methods work well for monochromatic images (such as gray-scale images) but the extension to multi-dimensional data such as color image data is still an open problem. One of the first extension of the structure tensor to multi-valued images was proposed by [Zenno \(1986\)](#), but later it was reported that channel-by-channel denoising is sufficient in the framework of partial differential equations, e.g., [Weickert \(1999\)](#). Coupling of the color channels were investigated in [Tschumperlé and Deriche \(2003\)](#) and decorrelation approaches to denoising have also been considered see, e.g., [Åström et al. \(2012\)](#). Explicitly modeling the structure of cyclic data, such as defined in specific color spaces, [Bergmann and Weinmann \(2016\)](#) presents a second order TV-type approach to denoising color images.

For a gray-scale image $u: \Omega \rightarrow \mathbb{R}$ defined on a domain $\Omega \subset \mathbb{R}^2$, the total variation measure is given by

$$TV(u) = \sup \left\{ \int_{\Omega} u \operatorname{div}(\varphi) \, dx : \varphi \in \mathcal{C}_c^1(\Omega, \mathbb{R}^2), \|\varphi\|_{\infty} \leq 1 \right\} \quad (1)$$

A function $u \in L^1(\Omega)$ belongs to the space of functions of bounded variation $BV(\Omega)$ if

$$\|u\|_{BV(\Omega)} = \|u\|_{L^1(\Omega)} + TV(u) < \infty. \quad (2)$$

$TV(u)$ given by (1) is a support function in the sense of convex analysis. Thus, combining $TV(u)$ with another (or more) convex functionals enables to apply a wide range of convex programming techniques. An early basic example is [Chambolle \(2004\)](#). Further common strategies include the primal-dual algorithm ([Chambolle and Pock, 2011](#)) and the Split-Bregman approach ([Goldstein and Osher, 2009](#)).

Next, we review generalizations of scalar TV to vector-valued and color images.

2.1. Color and vector-valued TV

Let $u: \Omega \rightarrow \mathbb{R}^d, u(x) = (u_1(x), \dots, u_d(x))^T$, denote a vector-valued image. Color images are represented by the three color components red, green and blue, i.e., $d = 3$. In this section we review some extensions of total variation to vector-valued and color images categorized in three main tracks: channel-by-channel, spectral approaches and decorrelation approaches. We briefly mention PDE-based models.

Channel-by-channel. The straightforward extension of TV to vector-valued color image regularization is to apply (1) channel-by-channel. However, as this naive approach neglects any channel-by-channel correlation one of the first extensions was to penalize color edges across channels as suggested by [Blomgren and Chan \(1998\)](#). They raised several important aspects highlighting the fact that the extension to color is a non-trivial task. First, they argued that the vector-valued TV should not penalize intensity edges, as there can be a shift in color but not in intensity. Secondly, they advocate that the corresponding TV-regularizer should be rotationally invariant in the image space, although this is disputed in [Ono and Yamada \(2014\)](#). [Blomgren and Chan \(1998\)](#) propose

$$TV_{BC}(u) = \sqrt{\sum_{i=1}^M TV(u_i)^2}, \quad (3)$$

with the TV term under the sum given by (1). However, applying this model to the problem of color image denoising has been shown to produce significant color smearing artifacts due to insufficient preservation of color edges. The reason of this effect is that the model fails to comprehend that the red, green and blue color components are in fact highly correlated. Thus, due to lacking any coupling between the color channels, the model produces suboptimal results w.r.t. to color consistency ([Goldluecke et al., 2012](#)).

[Bresson and Chan \(2008\)](#) considered a vector-valued extension of the scalar dual TV formulation. Based on work by [Chambolle \(2004\)](#) and [Fornasier and March \(2007\)](#), [Bresson and Chan \(2008\)](#) presented a coherent framework for vectorial total variation with a study of well-posedness. While their formulation generalizes Chambolle's dual of Blomgren's TV semi-norm (3), results still exhibit color smearing.

We refer to [Duran et al. \(2016\)](#) for an additional discussion on discrete vectorial total variation models. We remark that this underlines the complex nature of color image processing and researchers continued to propose alternative total variation color filtering models, as we will discuss below.

Spectral approaches. One of the first vectorial TV (VTV) schemes that explicitly take color information into account, was introduced by [Sapiro and Ringach \(1996\)](#). In an intensity image an edge is localized by changes in the image intensity. The novelty introduced by [Sapiro and Ringach \(1996\)](#) is that they exploited the metric imposed by the first fundamental form on the image domain, which couples the RGB-channel's derivatives, to indicate the presence of color edges. The resulting functional is given by

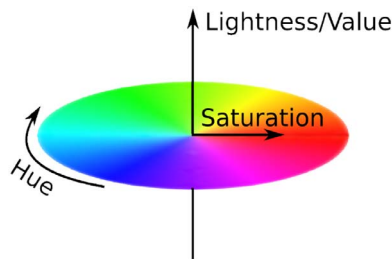


Fig. 2. An isoluminant disc of the double-opponent color space. Hue is an angular component describing the primary colors red, green, blue, and the opponent colors yellow, magenta and cyan and the corresponding colors transitions. Saturation describes the strength of the corresponding hue, and value gives the intensity with which the color is perceived. In the case of scalar valued (gray-scale images) the saturation is null and thus the hue plays no role. (For interpretation of the references to colour in this figure legend, the reader is referred to the web version of this article.)

$$TV_S(u) = \int_{\Omega} \sqrt{\lambda_+ - \lambda_-} dx, \quad (4)$$

where $\lambda_+ > \lambda_- \geq 0$ are the eigenvalues of the metric tensor.

Goldluecke and Cremers (2010) propose a vectorial total variation method based on the largest singular value (hence on the spectral norm) of the derivative matrix Du ,

$$TV_J(u) = \int_{\Omega} \sigma_1(Du) dx. \quad (5)$$

TV_J is closely related to TV_S with the difference that TV_J sets all singular values (except) the largest to zero. Although TV_J improves the signal-to-noise ratio, the visual appearance for the denoised results contains considerable color shimmering visible in homogeneous regions. Thus, despite a coupling between the color channels, the approach still may produce color artifacts.

Decorrelation transforms. Regularization via decorrelation transforms was suggested in e.g., Chan et al. (2001). A more recent approach to incorporating color into a total variation formulation was introduced by Ono and Yamada (2014). They propose a discrete norm incorporating a weight w between the intensity and chromaticity in the decorrelation transform O (see also (8),(9) below)

$$J_{TV}(u) = \|D_3 O u\|_1^w = w \|D_1 o_1\|_1 + \left\| \begin{pmatrix} D_1 o_2 \\ D_1 o_3 \end{pmatrix} \right\|_1 \quad (6)$$

where $\|x\|_1 = \sqrt{\sum_i x_i^2}$. D_1 is the derivative matrix for one channel and $D_3 = \text{Diag}(D_1, D_1, D_1)$ the three channel derivative matrix. The constant $w \in (0, 1)$ determines the weighting between the intensity and the chromaticity of the color space. A smaller w will penalize the chromaticity. This formulation, however, does not take into account that the subspace defined by (o_2, o_3) is not decorrelated but actually consists of the components hue and saturation. The framework does not respect the non-uniformity of the opponent space. As a consequence, direct regularizing on the chromaticity via an Euclidean distance metric violates the non-Euclidean structure of this opponent space. Furthermore, it is easy to construct scenarios where the image saturation changes independently of the hue, thus further motivating why they should be decomposed into hue and saturation (Munsell, 1905).

PDE-based models. There are many PDE-based models for color image filtering. We confine ourselves to referring to Åström et al. (2012); Tschumperlé and Deriche (2003); Weickert (1999) and to discussing the work of Chambolle (1994) who proposed a partial differential equation (PDE)-based anisotropic diffusion model. This model aims to solve the problem of color constancy (referring to the work by Hurlbert and Poggio (1998)). Although Chambolle (1994) did not present an energy-based total variation approach, his treatment of the color channels and their smoothing along the image gradient direction is relevant to our subsequent analysis. Chambolle (1994) proposes a PDE with directional diffusivity ξ defined as

$$\xi \perp ((u_2 - u_3) \nabla u_1 + (u_3 - u_1) \nabla u_2 + (u_1 - u_2) \nabla u_3) = 0, \quad (7)$$

reducing smoothing perpendicular to the gradients. The coupling between color channels is explicit: the difference of the intensity level of two color components affects the directional smoothing of the third channel. In practice, ξ is used in the heat equation to inhibit smoothing close to color edges. However, as noted by Sapiro and Ringach (1996), if two channels are equiluminant and if the third channel has an edge, this edge will remain unaffected by the filter.

Although these ideas were presented more than two decades ago, they did not attract much attention in the image processing community. We will see that our perceptual model is related to (7) in that our approach penalizes the pair-wise differences between the image derivatives, not the pair-wise intensity differences. In Section 4 we derive a color descriptor which couples the color channels in a natural way derived from the geometry of the double-opponent color transform. We will show that a color channel coupling similar to that of Chambolle (1994), in combination with related ideas to the geometric framework of Sapiro and Ringach (1996), results in a natural description of the image colorfulness.

3. Color

Color perception is a well studied area and researchers continue to propose color models. To use the “correct” color model is application dependent and a non-trivial problem. In this work we focus on the application of denoising. Next we briefly introduce established principles of color space design and recall some terminology.

3.1. Terminology

Some of the earliest works on color theory date back to the work by Newton (1671). In modern sciences, Albert Munsell is often accredited the notion color dimensions *hue*, *value* and *saturation* (Munsell, 1905). Fig. 2 illustrates the dimensions where hue is an angular component, value the intensity and saturation a radial component. For consistent use of the color terminology see The Commission Internationale de l’Eclairage (International Commission on Illumination, CIE) (CIE, 1987) and (Sharma, 2002). For further in-depth information on color image processing and the structure of color we refer to Sharma (2002). When we write intensity, we mean lightness, implying the monochromatic component black and its brightness, or simply, the image gray-scale component. When we write saturation we refer to the magnitude of the color vector orthogonal to the intensity, and hue refers to an angle ranging from 0 to 360° as illustrated in Fig. 2. During the last decades several color systems have been proposed to represent color, each considering different constraint sets. The next section reviews some of the more frequently referred color space representations.

3.2. Color space design

It is important to note when dealing with color theory that color is a subjective experience. In fact, one often thinks of color as wavelength of light. This is a misconception, however, since color is a result of neural processing in the human brain (Shevell, 2003, Ch. 4). This alludes to the difficulty of obtaining a quantitative and accurate description of color. Next, we list three major points that require consideration when determining suitable color space representations.

- **Color reproduction.** Color reproduction is the problem of reproducing color independent of display system. The Munsell system (Munsell, 1905), was the first standardization for color metrics widely accepted and later adopted by CIE in 1931. The recommendations set forth by CIE still continue to influence today’s color research (Sharma, 2002). Due to the subjective nature of color perception many color models have been proposed, however,

appropriate color space representation seems so far to be application dependent and no consensus has been reached. Due to the emerging technology of Internet and the large variety of imaging display systems and hardware limitations, a standardized RGB color space called sRGB was proposed for consistent image rendering over a wide range of devices (sRGB, 2003). Even up to present time, sRGB is a widely used color space on the world wide web. Also CIELAB is used for color reproduction due to its perceptual uniform structure and is mentioned next.

- **Perceptual uniformity.** The CIELAB color space was developed for perceptual uniformity. Color and perceptual uniformity, for image processing applications, implies that a perturbation in, e.g., hue, may influence a reference color to a different degree and may induce color artifacts for certain colors, but not for others. Perceptually, this is known to as the just-noticeable-difference and can be visualized via MacAdam ellipses (MacAdam, 1942). In reality it has been shown that the CIELAB is *almost* perceptually uniform, see Sharma (2002) and references therein. This motivates the use of non-Euclidean metrics, even in supposedly perceptually uniform cases, to determine the distance between colors. Due to the strong emphasis on perceptual uniformity the CIELAB color space is less suitable for rigorous mathematical treatment due to numerous discontinuities in its definition.
- **Hardware limitations.** Many color spaces were introduced as a consequence of technical and hardware limitations. Such a color space was the HSV (Hue, Saturation, Value) color space developed in the 1970 for applications related to color display systems (Joblove and Greenberg, 1978). The YCbCr/YPbPr color spaces were proposed for analog and digital television transmission, respectively. Furthermore, the YCbCr/YPbPr signal representation include non-linear mappings and chroma bandlimiting function to enable efficient transmission of the image signal (Poynton, 2003). One can also argue that the previously mentioned sRGB is part of this category. Due to the strong adaptation to efficient engineering requirements, color spaces in this category have not been subject to extensive research in the context of color image processing.

Next we present the double-opponent color space.

3.3. Double-opponent color representation

Recall that the most commonly used color space is the RGB color space. It consists of three components, r , g and b which are the Red, Green and Blue components. These components are uniformly spaced in $[0, 255]$ (or $[0, 1]$) depending on the chosen quantization. The r , g , b components are highly correlated, and thus image processing algorithms without explicit color adaptation introduce artificial colors and color smearing. To address this problem, a decorrelation transform is usually applied, converting the color space into the three components of intensity, saturation and hue¹.

The mapping from the decorrelated double-opponent space in the visual cortex to a physical stimuli is denoted via a function $\psi^{-1}: \mathbb{R}^3 \rightarrow \mathbb{R}^3$ defined by (10) below. We denote by, $u: \Omega \rightarrow \mathbb{R}^3$, the physical stimuli containing red, green and blue spectra. Furthermore, denote by the linear mapping

$$O: \mathbb{R}^3 \rightarrow \mathbb{R}^3, \quad u = (r, g, b)^T \mapsto Ou = o = (o_1, o_2, o_3)^T, \quad (8)$$

the transformation from the RGB color space to the double-opponent space where the matrix O is defined as (see Ebner (2007); Gao et al. (2013); Land (1983, 1986); Lenz and Latorre Carmona (2010)),

$$O = \begin{pmatrix} 1/\sqrt{3} & 0 & 0 \\ 0 & 1/\sqrt{6} & 0 \\ 0 & 0 & 1/\sqrt{2} \end{pmatrix} \begin{pmatrix} 1 & 1 & 1 \\ 1 & 1 & -2 \\ 1 & -1 & 0 \end{pmatrix}. \quad (9)$$

We note that this linear mapping has full rank. The matrix O actually describes a rotation and scaling of the RGB coordinate system. The opponent component o_1 is nothing else than the gray-scale value, o_2 is the subtraction of yellow (mixing red and green equals yellow) from blue and the last component o_3 is the subtraction of green from red, i.e., o_2 and o_3 consists of the opponent colors in the RGB color space and will henceforth be denoted as the chromaticity of a color.

The non-linear mapping to the hue (h), saturation (s) and intensity (L) representation of the decorrelated double-opponent space is given by

$$\psi: \mathbb{R}^3 \rightarrow \mathbb{R}^3, \quad o \mapsto c = (L, h, s)^T \quad (10)$$

where

$$L = o_1, \quad h = \arctan\left(\frac{o_2}{o_3}\right), \quad s = \left\| \begin{pmatrix} o_2 \\ o_3 \end{pmatrix} \right\|, \quad (11)$$

Let $\varphi: \mathbb{R}^3 \rightarrow \mathbb{R}^3$ denote the composition of the linear opponent transform (9) and the mapping $(o_1, o_2, o_3)^T \mapsto (L, h, s)^T$ just discussed above, then we define

$$\varphi: u \rightarrow \varphi(u) := \psi(Ou). \quad (12)$$

In the next section we compute the metric tensor associated with the mapping φ and investigates its encoded information.

4. Geometry of the double-opponent space

In this section we derive a color representation that allows for an intuitive interpretation of the double-opponent color space as components of the RGB-space. Subsequently we give an exposition on the information that this representation encodes.

4.1. Double-opponent metric tensor

Strictly speaking, in this work, we regard the RGB-space as a linear Riemannian manifold \mathcal{M} equipped with the metric (13), which is an inner product on the tangent space $T_u \mathcal{M}$ that smoothly varies with $u \in \mathcal{M}$. Since every tangent space $T_u \mathcal{M}$ can be identified with \mathcal{M} , however, it makes sense to regard the Riemannian metric (13) as inner product defined on the space itself. We refer, e.g., to Jost (2005) for background and further details.

Let $u = (u_1, u_2, u_3)^T = (r, g, b)^T$. The Euclidean inner product $\langle \cdot, \cdot \rangle$ on the Lhs -space induces via φ the pullback metric on the RGB-space given by

$$\langle u_1, u_2 \rangle_u := \langle D\varphi(u)u_1, D\varphi(u)u_2 \rangle = \langle u_1, G(u)u_2 \rangle, \quad (13a)$$

$$G(u) := (D\varphi(u))^T D\varphi(u) = (g_{ij}(u))_{i,j=1,2,3} \quad (13b)$$

where the Jacobian $D\varphi$ and the corresponding metric tensor G are computed as

$$D\varphi(u) = \frac{1}{\sqrt{3}} \begin{pmatrix} 1 & \frac{3}{f} \frac{\alpha}{\|\alpha\|} & \frac{1}{f} \beta \end{pmatrix}^T, \quad (14a)$$

$$G(u) = \frac{1}{3} \left(I + \frac{9}{f^4} \alpha \alpha^T + \frac{1}{f^2} \beta \beta^T \right), \quad (14b)$$

with

$$\alpha = \alpha(u) := (\alpha_1, \alpha_2, \alpha_3)^T = (b - g, r - b, g - r)^T, \quad (15a)$$

$$\beta = \beta(u) := (\beta_1, \beta_2, \beta_3)^T = (b + g - 2r, b + r - 2g, r + g - 2b)^T, \quad (15b)$$

¹ The transformation to these components is *not* equivalent with the HSV color space. Although, the interpretation of the components are similar.

$$f^2 = f^2(u) = \|\alpha\|^2 = 2(b^2 - bg - br + g^2 - gr + r^2). \quad (15c)$$

To capture the image color variations we decompose the metric tensor G into its eigenvalue decomposition and obtain the eigenvalues

$$\Lambda = \frac{1}{3}I + \text{Diag}\left(0, \frac{3}{f^2}, 1\right) \quad (16)$$

which have the associated non-normalized eigenvectors $\mathbf{1}$, α , β given in (15). Furthermore, one easily verifies the relations

$$\alpha \perp \beta, \quad u \perp \alpha, \quad \alpha \times \beta = f^2 \mathbf{1}, \quad \langle u, \beta \rangle = f^2, \quad \|\beta\|^2 = 3 \|\alpha\|^2. \quad (17)$$

where \times denotes the cross product and \perp indicates that the components are orthogonal.

In the next section we study the information encoded in the eigenvalues (16), in particular f^2 will be subject for this analysis

$$\gamma = f^2 = u^\top P u, \quad P = \begin{pmatrix} 2 & -1 & -1 \\ -1 & 2 & -1 \\ -1 & -1 & 2 \end{pmatrix} \geq 0. \quad (18)$$

where P is a symmetric and positive semi-definite matrix.

Sapiro and Ringach (1996) also exploited the first fundamental form but in Euclidean space and concluded that the tensor's eigenvalues capture the color edge information. Here we instead use the principal directional change obtained from the eigendecomposition of the double-opponent metric tensor. And our focus is on γ of (18). Similarly to Sapiro and Ringach (1996), the interpretation is that a large eigenvalue of the tensor will indicate the presence of image color. Next, we justify and elaborate this statement in the next section while investigating the information encoded in γ .

4.2. Encoded information

This section investigates the information encoded in the metric tensor, decomposed into an eigensystem as in the previous section. The derived γ describes the *colorfulness* of an image, and in the next section we formulate an energy model that explicitly preserve discontinuities in γ . We identify the following relation

$$\begin{aligned} \gamma(u) &= u^\top P u = (b - r)^2 + (r - g)^2 + (g - b)^2 \\ &= \|u^\top C_1\|^2, \quad C_1 = \begin{pmatrix} 1 & -1 & 0 \\ 0 & 1 & -1 \\ -1 & 0 & 1 \end{pmatrix}. \end{aligned} \quad (19)$$

Note that $P = C_1 C_1^\top$ (cmp. (18)) and that $\gamma = 3s^2$. The coefficients of $C_1 u$ have previously appeared in Chambolle (1994) by Chambolle and in Felsberg et al. (2015), however in the context of visual feature descriptors.

Proposition 4.1. *The function, γ in (19), has the properties (P1) $\gamma(u + c\mathbf{1}) = \gamma(u)$ and (P2) $\gamma(cu) = c^2\gamma(u)$, where c is a constant.*

Proof. The result follows immediately from (19). \square

The above result yields the following interpretation of the γ -function: a) (P1) shows that γ is invariant to intensity shifts. b) (P2) shows that γ has a quadratic dependency on intensity changes. c) It follows from a) that γ depends on color changes. d) It follows from b) that γ depends on color shifts. Under constant intensity, γ captures change of color as illustrated by Fig. 3 (a), (b). In this figure we show equilibrium discs at constant intensity along with the corresponding response of γ . It is clearly visible that γ describes the intrinsic color structure of the color space as there is a stronger response for highly saturated colors. In the lower half of the intensity range we predominantly detect the primary colors red, green and blue. As the intensity increases, γ shows primary responses from yellow, cyan and magenta. The intensity axis is located in the center of these discs and, as expected, we do not obtain a value of colorfulness. We give some

examples of γ -responses from natural images in Fig. 4.

The *geometric interpretation* of γ is illustrated as an example via the r-g-component. The other two color difference terms follow with similar reasoning. We know that the color yellow, y , is composed as a sum of red and green, i.e., $y = r + g$, and written in vector form we have $r - g = (1, -1, 0)^\top$ and $y = r + g = (1, 1, 0)^\top$. We see that yellow is perpendicular to the difference $r - g$, i.e., $y \perp (r - g) = 0$. This is illustrated in Fig. 3 (c). Analogous argument hold for the other terms of γ , i.e., $b - r$ is orthogonal to magenta, and $g - b$ orthogonal to cyan. In this way γ covers the RGB space. Moreover, as γ describes the color structure, preserving its edge information prevents color distortion in the filtering process. Based on this analysis, we are now prepared to introduce the general variational formulation.

5. General variational formulation

Let $u = [u_R^\top, u_G^\top, u_B^\top]^\top \in \mathbb{R}^{3N}(\Omega)$ represent a color image on the domain Ω with stacked color channels. N is the number of pixels in one image channel. Also, let $g \in \mathbb{R}^{3N}$ be the corresponding noisy data. We define the discrete image gradient for *one* channel as $D_1 = \begin{bmatrix} D_x \\ D_y \end{bmatrix} \in \mathbb{R}^{2N \times N}$, $D_x, D_y \in \mathbb{R}^{N \times N}$ and subscript denotes the forward finite difference operator in x and y directions, respectively. Furthermore, we let $i \in \mathbb{N}^+$ s.t. $I_i \in \mathbb{R}^{i \times i}$ denotes the identity matrix. In this notation, the three channel derivative matrix for a color image is $D^{(1)} = D_1 \otimes I_3 \in \mathbb{R}^{6N \times 3N}$ where \otimes is the Kronecker product and

$$D^{(1)}u: \mathbb{R}^{3N} \rightarrow \mathbb{R}^{6N} \quad (20)$$

is the derivative matrix for the three channels.

5.1. Energy

Channel-by-channel filtering of the RGB space is prone to introduce color artifacts (Blomgren and Chan, 1998; Bresson and Chan, 2008). On the other hand, purely decorrelating the color channels without considering the geometry is also sub-optimal, see results in, e.g., Ono and Yamada (2014); Sapiro and Ringach (1996). We propose a two-component regularizer: one component performs channel-by-channel filtering penalizing *all* intra-channel content and one component which explicitly targets the color information. The color specific prior defines a natural inter-channel coupling from the geometry of the double-opponent space, realized through

$$C \in \mathbb{R}^{3N \times 3N}, \quad C = C_1 \otimes I_N \quad (21)$$

where C_1 corresponds to (19).

For $M \in \mathbb{N}$ let $m \in \{1, \dots, M\}$, then we define $\alpha, \beta \in \mathbb{R}_+^M$ and $p, q \in \mathbb{R}^M(0, 2)$, such that α, β, p, q are vectors with components indexed by subscript, e.g., α_m . We let $s \in (0, 2)$ and by $\|x\|_p^s$ we mean

$$\|x\|_p^s = \sum_{i=1}^{3N} |x_i|^p. \quad (22)$$

The energy we introduce and study in this work is defined as the *non-convex* optimization problem

$$\min_u \left\{ E(u) = \frac{1}{s} \|Ku - g\|_s^s + \sum_{m=1}^M \left(\frac{\alpha_m}{p_m} \|D^{(m)}u\|_{p_m}^{p_m} + \frac{\beta_m}{q_m} \|D^{(m)}Cu\|_{q_m}^{q_m} \right) \right\}, \quad (23)$$

where $D^{(m)}$ is the m -order derivative matrix. When $m = 1$ we have a *first-order* energy and if $m = 2$, we have a second-order energy and so forth. To be explicit, we give the derivative matrix for the first and second order cases

$$D^{(1)} = \begin{pmatrix} D_x \\ D_y \end{pmatrix} \quad (24a)$$

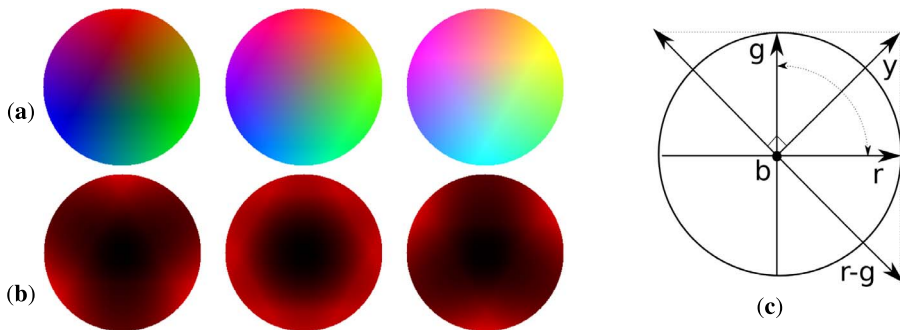


Fig. 3. (a) Color discs with corresponding response of γ , (19), in (b). The largest magnitude (red color) is obtained at the primary colors (red, green and blue) and the opponent colors (yellow, cyan and magenta). As expected, the response on the intensity axis (center of discs) is 0 (black). (c) Interpretation of the vector $r - g$ as an orthogonal component to yellow. (For interpretation of the references to colour in this figure legend, the reader is referred to the web version of this article.)

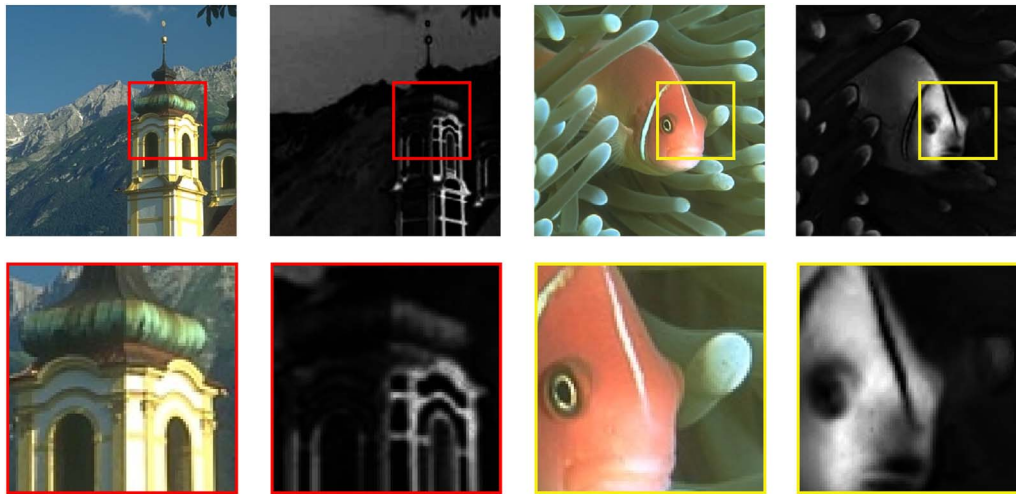


Fig. 4. Detected color structure in real images extracted by γ . In these examples, primary colors such as red, green and blue and the opponent color yellow are well characterized. (For interpretation of the references to colour in this figure legend, the reader is referred to the web version of this article.)

and

$$D^{(2)} = \begin{pmatrix} D_{xx} \\ D_{xy} \\ D_{yx} \\ D_{yy} \end{pmatrix} \quad (24b)$$

where subscript denotes the derivative in x and y -directions, respectively. The operator $K \in \mathbb{R}^{3N \times 3N}$ in (23) is the identity matrix in the case of denoising or a blurring matrix in the case of deconvolution. Since the product Cu is now the pair-wise mixture of color channels, it means that DCu is the pair-wise mixture of the channel gradients, i.e., DCu penalizes color opponent gradients in y , c and m , and Du penalizes the primary colors r , g and b . With $m > 1$ we have a natural definition of higher-order total variation. Although C is a constant matrix, it is non-trivial to minimize E due to its inherent non-convexity when either of p , q , $s \in (0, 1)$. For this reason, we adopt a half-quadratic formulation presented next.

5.2. Half-quadratic formulation

Alternatives to the HQA (Geman and Yang, 1995) include, e.g., fitting of auxiliary variables (Cohen, 1996) which, however for practical applications, relies on the efficient evaluation of a conjugate function. One may also consider lagged fix-point formulations (Chan and Mulet, 1999), in this case one would impose regularity to obtain a differentiable energy and prove that there exists a convergent fixed-point algorithm. Instead, the HQA algorithm is particularly suited to optimize E since we obtain a computationally very efficient scheme. Furthermore, identifying that the HQA can be written as an instance of a majorize-minimize scheme we also show that the HQA convergences to a stationary point corresponding to a minimum. We make use of the following result to optimize our energy

Lemma 5.1. (HQA p -norm (Chan and Liang, 2014)) Let $p \in (0, 2)$ and $t \in (\mathbb{R} \setminus \{0\})$, then

$$\|t\|^p = \min_{v>0} \left\{ vt^2 + \frac{1}{\xi v^\eta} \right\} \quad (25)$$

where $\eta = \frac{p}{2-p}$, $\xi = \frac{2^{2/(2-p)}}{(2-p)p^{p/(2-p)}}$, and the minimum is obtained at

$$v^* = \frac{p}{2} |t|^{p-2}. \quad (26)$$

The energy E in (23) is not differentiable and not convex. To apply the HQA, we make use of the mollified energy E_ϵ and set $\|x\|_{\eta,\epsilon}^\eta = \sum_{i=1}^M (|x_i| + \epsilon)^\eta = \sum_{i=1}^M |x_i|_\epsilon^\eta$ and $0 < \eta < 2$. Now, the energy $E_\epsilon(u)$ is differentiable but not convex, therefore the direct optimization problem

$$u^{k+1} = \min_u E_\epsilon(u) \quad (27)$$

may result in a locally optimal solution. The HQA optimization problem takes the form

$$\min_u \left\{ E_\epsilon(u) = \sum_{i=1}^{3N} \frac{1}{s} \min_{z>0} \left(z |K_i u - g_i|_\epsilon^2 + \frac{1}{\xi_s z_i^{\alpha_s}} \right) + \sum_{m=1}^M \left[\frac{\alpha_m}{p_m} \min_{v_m>0} \left(v_{i,m} |D_i^{(m)} u|_\epsilon^2 + \frac{1}{\xi_{p_m} v_{i,m}^{\alpha_{p_m}}} \right) + \frac{\beta_m}{q_m} \min_{w_m>0} \left(w_{i,m} |D_i^{(m)} C u|_\epsilon^2 + \frac{1}{\xi_{q_m} w_{i,m}^{\alpha_{q_m}}} \right) \right] \right\} \quad (28a)$$

$$= : \min_{u, v_1>0, \dots, v_m>0, w_1>0, \dots, w_m>0, z>0} \mathcal{L}(u, v, w, z) \quad (28b)$$

now convex separately in u and in z, v, w , respectively. We use subscript “ i ” to denote the i 'th row (or component) of a matrix (or vector). By using Lemma 5.1 we formulate an alternating minimization strategy where the update equations for the auxiliary variables are given by

$$z^{k+1} = \frac{s}{2} |Ku^k - g|_e^{s-2} \quad (29a)$$

$$(v_m^{k+1}, w_m^{k+1}) = \left(\frac{p_m}{2} |D^{(m)} u^k|_e^{p_m-2} \right)^\top, \quad m = 1, \dots, M \quad (29b)$$

and the norm is taken component-wise. The update equation for the convex subproblem u^{k+1} is obtained by minimizing

$$u^{k+1} = \arg \min_u \sum_{i=1}^{3N} \frac{1}{s} z_i^{k+1} |K_i u - g|_e^2 + \sum_{m=1}^M \left(\frac{\alpha_m v_{i,m}^{k+1}}{p_m} |D_i^{(m)} u|_e^2 + \frac{\beta_m w_{i,m}^{k+1}}{q_m} |D_i^{(m)} C u|_e^2 \right) \quad (30)$$

Convergence analysis. The main idea of the following convergence result is to express the HQA as an instance of the majorize-minimize (MMA) algorithm (Chan and Mulet, 1999). Once we establish the link between the HQA and the MMA we can show convergence of our algorithm.

Assume there exists a function Φ such that

$$\min_u E_\varepsilon(u) = \min_u \Phi(u) \quad (31)$$

and to show that the HQA formulation is of the MMA-type we consider the optimization problem

$$u^{k+1} = \arg \min_u \mathcal{F}(u, u^k). \quad (32)$$

If there exists a function Φ such that \mathcal{F} satisfies

$$\mathcal{F}(u, u^k) \geq \Phi(u), \quad \text{for } \forall u \in \mathbb{R}^n \quad (33a)$$

$$\mathcal{F}(u, u^k) = \Phi(u), \quad \text{for } u = u^k \quad (33b)$$

$$\nabla_u \mathcal{F}(u, u^k) = \nabla \Phi(u), \quad \text{for } u = u^k \quad (33c)$$

With \mathcal{L} from (28b) and taking into account that $v^{k+1}, w^{k+1}, z^{k+1}$ depend on u^k , we define:

$$\mathcal{F}(u, u^k) := \mathcal{L}(u, v^{k+1}, w^{k+1}, z^{k+1}) \quad (34)$$

and have the following result

Proposition 5.2 (MMA). *The optimization problem (30), stemming from the HQA, is an instance of MMA with \mathcal{F} defined as in (34).*

Proof. We adopt the solution strategy introduced in Chan and Liang (2014). The first step is to start by substitute (29) into (34) and get expression (35).

$$\begin{aligned} \mathcal{F}(u, u^k) &= \sum_{i=1}^{3N} \frac{1}{s} \left(\frac{s}{2} |K_i u^k - g_i|_e^{s-2} |K_i u - g_i|_e^2 + \frac{(2-s)}{2} |K_i u^k - g_i|_e^s \right) \\ &+ \sum_{m=1}^M \left[\frac{\alpha_m}{p_m} \left(\frac{p_m}{2} |D_i^{(m)} u^k|_e^{p_m-2} |D_i^{(m)} u|_e^2 + \frac{(2-p_m)}{2} |D_i^{(m)} u^k|_e^{p_m} \right) \right. \\ &\left. + \frac{\beta_m}{q_m} \left(\frac{q_m}{2} |D_i^{(m)} C u^k|_e^{q_m-2} |D_i^{(m)} C u|_e^2 + \frac{(2-q_m)}{2} |D_i^{(m)} C u^k|_e^{q_m} \right) \right] \end{aligned} \quad (35)$$

Then we set $\mathcal{F}(u = u^k, u^k)$ which results in

$$\begin{aligned} \mathcal{F}(u^k, u^k) &= \sum_{i=1}^{3N} \frac{1}{2} |K_i u^k - g_i|_e^s + \sum_{m=1}^M (\alpha_m |D_i^{(m)} u^k|_e^{p_m} + \beta_m |D_i^{(m)} C u^k|_e^{q_m}) \\ &= \Phi(u^k) \end{aligned} \quad (36)$$

where Φ was defined in (31) and establishes condition (33b). In order to show condition (33a), i.e., that \mathcal{F} forms an upper envelope of $\Phi(u)$ we identify that (35) can be expressed with Young's inequality. Then under the condition $1/a + 1/b = 1$ we have that

$$\frac{g^a}{a} + \frac{h^b}{b} \geq gh. \quad (37)$$

We set $\xi(u) = |K_i u - g_i|_e$

$$g = \xi(u^k)^{\frac{(s-2)s}{2}} \xi(u)^s \quad (38a)$$

$$h = \xi(u^k)^{\frac{(2-s)s}{2}} \quad (38b)$$

and let $a = \frac{s}{2}, b = \frac{2}{2-s}$, which verifies the inequality

$$\begin{aligned} \frac{s}{2} |K_i u^k - g_i|_e^{s-2} |K_i u - g_i|_e^2 + \frac{(2-s)}{2} |K_i u^k - g_i|_e^s &\geq |K_i u - g_i|_e^s, \\ i = 1, \dots, 3N \end{aligned} \quad (39)$$

With an analogous reasoning of the remainder of (35) components we have that $\mathcal{F}(u, u^k) \geq \Phi(u)$, i.e., condition (33a) is fulfilled. Finally, one easily verifies that $\nabla_u \mathcal{F}(u, u^k) = \nabla \Phi(u)$ at $u = u^k$, thus (33c) holds. This shows that $\mathcal{F}(u, u^k)$ is a majorizing function of (28). \square

Theorem 5.3 (Convergence). *Given a sequence $\{u^k\}$ generated by HQA, then (i) $\Phi(u^k)$, (36), is monotonically decreasing and convergent and (ii) $\lim \|u^k - u^{k+1}\|_e = 0$ as $k \rightarrow \infty$.*

Proof. The first and second order derivatives of \mathcal{F} are

$$\begin{aligned} \nabla_u \mathcal{F}(u, u^k) &= \sum_{i=1}^{3N} \frac{1}{s} z_i^{k+1} K_i^\top (K_i u - g_i) + \sum_{m=1}^M \frac{2\alpha_m v_{i,m}^{k+1}}{p_m} (D^{(m)})^\top D_i^{(m)} u \\ &+ 2 \frac{\beta_m w_{i,m}^{k+1}}{q_m} (D^{(m)} Q)^\top D_i^{(m)} Q u \end{aligned} \quad (40)$$

and

$$\begin{aligned} \nabla_u^2 \mathcal{F}(u, u^k) &= \frac{1}{s} \sum_{i=1}^{3N} z_i^{k+1} K_i^\top K_i + \sum_{m=1}^M \frac{2\alpha_m v_{i,m}^{k+1}}{p_m} (D^{(m)})^\top D^{(m)} \\ &+ 2 \frac{\beta_m w_{i,m}^{k+1}}{q_m} (D^{(m)} Q)^\top D^{(m)} Q \end{aligned} \quad (41)$$

where the latter matrix is positive semidefinite independently of u . Thus, \mathcal{F} is convex in u . Moreover, by (32) and (33),

$$\Phi(u^{k+1}) \leq \mathcal{F}(u^{k+1}, u^k) \leq \mathcal{F}(u^k, u^k) = \Phi(u^k). \quad (42)$$

From this it is immediate that

$$\lim_{k \rightarrow \infty} \Phi(u^k) - \Phi(u^{k+1}) = 0 \quad (43)$$

as Φ is bounded from below by 0. To show the convergence of u^k , we consider the Taylor expansion of $\mathcal{F}(u, u^k)$ at u^{k+1}

$$\mathcal{F}(u, u^k) = \mathcal{F}(u^{k+1}, u^k) + \frac{1}{2} (u - u^{k+1})^\top \nabla^2 \mathcal{F}(u, u^k) (u - u^{k+1}) \quad (44)$$

where the first-order term on the right-hand side vanishes due to the optimality condition of (32). Note that higher-order differentials $\nabla_u^{(n)} \mathcal{F}$, $n > 2$ vanish. Minimizing the right-hand side with respect to u and then setting $u = u^k$, we obtain

$$\mathcal{F}(u^k, u^k) \geq \mathcal{F}(u^{k+1}, u^k) + \frac{\xi}{2} \|u^k - u^{k+1}\|_e^2 \quad (45)$$

where ξ is positive and is the minimum eigenvalue of $\nabla_u^2 \mathcal{F}$. Consequently,

$$\mathcal{F}(u^k, u^k) - \mathcal{F}(u^{k+1}, u^k) \geq \frac{\xi}{2} \|u^k - u^{k+1}\|_e^2 \geq 0, \quad (46)$$

with the left-hand side converging to 0 due to (42) and (43). \square

Based on the identification with a MMA, we have shown convergence and existence of a solution for the corresponding HQA. Although, this result is significant, we required a mollifier, a constant offset ε in the denominator. This parameter regularizes the energy and thus introduces smoothness, albeit being small, it yields a smoother solution than desired. In the numerical evaluation we implement the above energy with an iterative Split-Bregman scheme and we obtain stable updates for ε as small as 10^{-20} , which we also used in the numerical evaluation. Next, we study the natural selection of first order derivative ($m = 1$), quadratic data term ($s = 2$) and corresponding vectorial total variation regularization ($p, q = 1$) with the same channel coupling matrix as in the HQA. In this case we do not require a mollification and we show that the corresponding minimizer resides in the space of vectorial bounded variation and is unique.

5.3. First-Order VTV

As a special instance of the general variational formulation (23) we study the existence of a solution of a *non-mollified* vectorial total variation term. Consequently we are not required to use the HQA. In this section we will also use a continuous formulation which is more efficient for this purpose, as such, we use the coupling matrix $C_1 \in \mathbb{R}^{3 \times 3}$ defined in (19).

In the following, let be the *vectorial gradient* of a color image in the generalized sense as discussed in connection with eq. (1). Then we define $p = (p_1, p_2, p_3) \in C_c^1(\Omega; \mathbb{R}^{2 \times 3})$ with $\text{Div}(p) = (\text{div}(p_1), \text{div}(p_2), \text{div}(p_3))^T$.

Definition 5.1 (*Double-opponent VTV*). The double opponent regularizer is defined as

$$J_{OPP}(u) := \int_{\Omega} \|\nabla C_1 u\| \quad (47a)$$

$$:= \sup_{\|p\|_{\infty} \leq 1} \left\{ \int_{\Omega} \langle C_1 u, \text{Div}(p) \rangle dx \right\} \quad (47b)$$

where $\|p\|_{\infty} = \max\{\|p_1\|, \|p_2\|, \|p_3\|\}$.

Next, we show that the regularizer J_{OPP} is convex, invariant to rotation and intensity shift of the color space.

Theorem 5.4 (*Invariance and convexity*). J_{OPP} is rotationally and intensity invariant, 1-homogeneous and convex.

Proof. Rotational invariance follows from the isotropy of the feasible set of the dual variable p , that is $\|p\|_{\infty} = \|(Rp_1, Rp_2, Rp_3)\|_{\infty} \leq 1 \Rightarrow \|(Rp_1, Rp_2, Rp_3)\|_{\infty} \leq 1$, for any orthogonal matrix R . As a consequence of property (P1) and (P2) of Prop. 4.1, J_{OPP} is invariant to intensity shifts, and the relation $J_{OPP}(cu) = cJ_{OPP}(u)$ is immediate, for any positive constant $c > 0$. Finally, convexity follows from the definition of J_{OPP} as pointwise supremum of affine functions. \square

The non-mollified first-order energy of (23), with a convex data-term, is defined as

$$\min_u \left\{ E(u) = \frac{\mu}{2} \|Ku - g\|_{L^2(\Omega)}^2 + \alpha \sum_{i=1}^3 \text{TV}(u_i) + \beta J_{OPP}(u) \right\} \quad (48)$$

where $\mu, \alpha, \beta > 0$. **Existence of solution.** Next we show that the variational approach (48) is well posed.

Lemma 5.5 (*Bounded variation*). Let $u \in BV(\Omega; \mathbb{R}^3)$ then $C_1 u \in BV(\Omega; \mathbb{R}^3)$.

Proof. Transposing the matrix C_1 in the integrand of (47b) shows that $J_{OPP}(u)$ is the support function of u with respect to the image of the unit ball $\{p: \|p\|_{\infty} \leq 1\}$ under the linear mapping $C_1^T \circ \text{Div}$. The claim then follows from the assumption $u \in BV(\Omega; \mathbb{R}^3)$. \square

As a consequence, the objective function $E(u)$ (48) is well defined. We next show that there is a unique color image u minimizing $E(u)$.

Theorem 5.6 (*Uniqueness and existence of solution*). Let $g \in L^{\infty}(\Omega; \mathbb{R}^3)$ and $u \in BV(\Omega; \mathbb{R}^3)$. Then there exists a unique minimizer u^* of $E(u)$ given by (48).

Proof. We adapt and sketch a standard proof pattern from Attouch et al. (2014). Due to $g \in L^{\infty}(\Omega; \mathbb{R}^M)$, we may assume that all admissible u are uniformly bounded in the sense that $|u_i(x)| \leq \|g_i\|_{L^{\infty}(\Omega)}$, $i = 1, 2, 3$, $\forall x \in \Omega$. Let $(u_n)_{n \in \mathbb{N}}$ be a minimizing sequence with respect to $E(u)$. Then, after passing to a subsequence $(u_{n_k})_{k \in \mathbb{N}}$, there exists a $u^* \in BV(\Omega; \mathbb{R}^3)$ with $u_{n_k} \rightarrow u^*$ strongly in $L^1_{loc}(\Omega; \mathbb{R}^3)$, $\nabla(u_{n_k}) \rightarrow \nabla u^*$ in an appropriate weak sense, and $J_{OPP}(u_{n_k}) \rightarrow J_{OPP}(u^*)$ in view of Lemma 5.5. It follows from Fatou's lemma and the lower-semicontinuity of $E(u)$ that u^* minimizes $E(u)$, whereas uniqueness of u^* is a consequence of the strict convexity of $E(u)$ due to the data term of (48). \square

Next, we derive an efficient numerical scheme which optimizes our proposed energies.

6. Implementation and optimization

We briefly comment on convex programming techniques that are relevant to our approach. Then we detail our implementation of a specific technique embedded into the half-quadratic regularization approach.

6.1. TV and convex programming

There exists numerous methods to minimize the total variation semi-norm. A very popular approach is the primal-dual iteration from Chambolle and Pock (2011); Chan et al. (1999). Related algorithms include the Split Bregman method (Goldstein and Osher, 2009), augmented Lagrangian methods (Wu and Tai, 2010) and the alternating direction method of multipliers (ADMM) (Wahlberg et al., 2012). The Split-Bregman technique has been shown to be equivalent to ADMM in the case of a linear constraint set (Esser, 2009). Further connections between these methods are discussed in (Wu and Tai, 2010).

An evaluation of these algorithms in connection with our approach is beyond the scope of this paper. We adopted the Split-Bregman algorithm (Goldstein and Osher, 2009) as an established technique and incorporated it as subroutine of our half-quadratic regularization approach, without claiming that this is the best possible choice.

6.2. Optimization via Split-Bregman and HQA

With the notation introduced in Section 5 above, and with the discretized channel matrix $C \in \mathbb{R}^{3N \times 3N}$ (see (21)) we write the discretized form of (23) as the optimization problem

$$\min_{u, d, e} \frac{\mu}{2} \|Ku - g\|_2^2 + \sum_{m=1}^M (\alpha \|d_m\|_p^p + \beta \|e_m\|_q^q) \quad (49a)$$

$$\text{s.t. } d_m = D^{(m)} u, \quad e_m = D^{(m)} C u. \quad (49b)$$

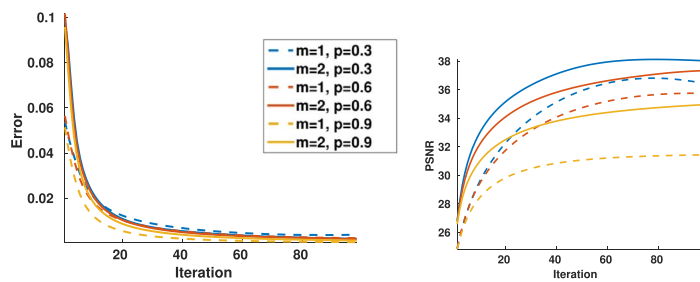
Let $\|v\|_i^2 := \langle v, H v \rangle$ be a weighted Euclidean norm and $d = (d_1^T, \dots, d_m^T)^T, e = (e_1^T, \dots, e_m^T)^T$. Let

$$D = (\text{vec}(D^{(1)})^T, \dots, \text{vec}(D^{(m)})^T)^T \quad (50)$$

(cf. (24)) and set

$$B(u, b, d, e) := \begin{pmatrix} d \\ e \end{pmatrix} - \begin{pmatrix} D \\ DC \end{pmatrix} u - b. \quad (51)$$

Applying the Split Bregman approach yields the iteration



(a) Normalized difference between two consecutive updates in the iterative update (58) computed as (59). (b) PSNR value of the current iterate u^k . The second order VTV ($m = 2$) consistently results in improved PSNR values.

$$(u^{k+1}, d^{k+1}, e^{k+1}) = \min_{u,d,e} \frac{\mu}{2} \|Ku - g\|_2^2 + \|d\|_p^p + \|e\|_q^q + \frac{1}{2} \|B(u, b, d, e)\|_H^2, \quad (52a)$$

$$b^{k+1} = b^k + \begin{pmatrix} D \\ DC \end{pmatrix} u^{k+1} - \begin{pmatrix} d^{k+1} \\ e^{k+1} \end{pmatrix}. \quad (52b)$$

In the cases of $p = 1$ and/or $q = 1$ we apply the shrinkage operator to minimize d, e , respectively. When p, q are in the non-convex range $(0, 1)$, we use the HQA in Lemma 5.1 and obtain the point-wise quadratic update step

$$(d^{k+1}, e^{k+1}) = \min_{d,e} v^{k+1} d^2 + w^{k+1} e^2 + \frac{1}{2} \|B(u^{k+1}, b^k, d, e)\|_H^2, \quad (53a)$$

$$(v^{k+1}, w^{k+1}) = \left(\frac{p}{2} \left| d^k \right|^{p-2}, \frac{q}{2} \left| e^k \right|^{q-2} \right), \quad (53b)$$

which is strictly convex in both d and e . Since (53) is defined point-wise, we get the optimality condition,

$$2 \begin{pmatrix} v^{k+1} d \\ w^{k+1} e \end{pmatrix} + \begin{pmatrix} \alpha & 0 \\ 0 & \beta \end{pmatrix} \begin{pmatrix} d \\ e \end{pmatrix} - \begin{pmatrix} D \\ DC \end{pmatrix} u^k - b = 0 \quad (54)$$

and the closed-form update-expression

$$\begin{pmatrix} d^{k+1} \\ e^{k+1} \end{pmatrix} = \begin{pmatrix} (Du^k + b_1)/(1 + 2v^{k+1}/\alpha) \\ (DCu^k + b_2)/(1 + 2w^{k+1}/\beta) \end{pmatrix}. \quad (55)$$

The optimization problem w.r.t. u is solved iteratively by

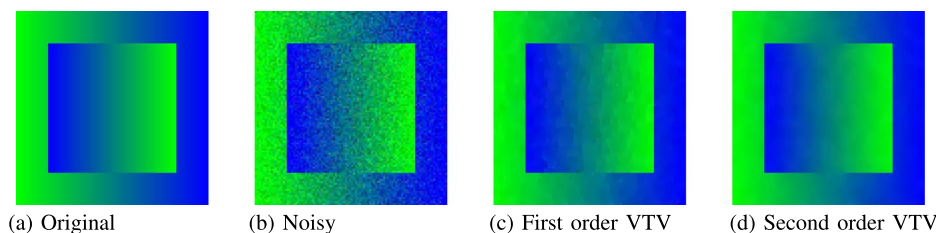
$$u^{k+1} = \min_u \frac{\mu}{2} \|Ku - g\|_2^2 + \frac{1}{2} \|B(u, b^k, d^k, e^k)\|_H^2. \quad (56)$$

In (56), we set $b = [b_1^T, b_2^T]^T$ for notational convenience and compute

$$\begin{aligned} \mu K^T(Ku^{k+1} - g) - \alpha D^T(d^k - Du^{k+1} - b_1^k) - \beta (DC)^T(e^k - DCu^{k+1} - b_2^k) \\ = 0 \end{aligned} \quad (57)$$

which gives the update step

$$\begin{aligned} (\mu K^T K + \alpha D^T D + \beta (DC)^T (DC)) u^{k+1} = \mu K^T g + \alpha D^T (d^k - b_1^k) \\ + \beta (DC)^T (e^k - b_2^k). \end{aligned} \quad (58)$$



(a) Original (b) Noisy (c) First order VTV (d) Second order VTV empirical convergence and PSNR values are shown in Fig. 5. (For interpretation of the references to colour in this figure legend, the reader is referred to the web version of this article.)

Fig. 5. Empirical convergence (a) of the image data in Fig. 6. The numerical scheme is implemented as presented in Section 6 and the trend of the corresponding PSNR curves are shown in (b). The regularization parameters were set as $\mu = 80, \alpha_1 = \beta_1 = 2$ for first order VTV. In the second order case we additionally set $\alpha_2 = \beta_2 = 1$.

Our experiments confirm the observation of Goldstein and Osher (2009) that only computing an approximate solution accelerates the overall iterative scheme without compromising convergence. Consequently, we merely apply few conjugate gradient iterative steps to compute u^{k+1} . This is computationally cheap since all matrices involved are sparse.

Finally, we iterate the steps (58), (53b), (55) and (52b) until we satisfy the stopping criterion

$$\|u^k - u^{k+1}\|_2^2 / \|u^{k+1}\|_2^2 < 0.9 \sqrt{3N\sigma^2} / 255^2, \quad (59)$$

where σ is the noise level standard deviation. This numerical scheme gives stable updates even when ε is very small. In the experimental evaluation we fixed $\varepsilon = 10^{-20}$.

7. Applications

We apply our approach to color image denoising, inpainting and deblurring. All images were normalized to the range $[0, 1]$ given in an 8-bit representation. In addition to a qualitative evaluation we include the measures peak signal-to-noise ratio (PSNR), the structural similarity index (SSIM) (Wang et al., 2004) and the CIEDE 2000 which is a measure of color consistency (Sharma et al., 2005). We consider two denoising scenarios. One synthetic case where the image data consist of piecewise affine regions. The other scenario concerns the denoising of natural images.

7.1. Synthetic image, convergence rate

The synthetic image is isoluminant and therefore presents a particular challenge due to the absence of gray-scale edges. Fig. 5 shows the empirical convergence rate of our approach for first ($m = 1$) and second ($m = 2$) order VTV for the noisy image corrupted by normally distributed noise on the r, g and b components with standard deviation 10 in Fig. 6. For each parameter setting the second order VTV shows improved PSNR values which correlates with the visual impression of the final result images in Fig. 6 (c) and (d), respectively.

7.2. Denoising of natural images

The aim of this section is to illustrate differences between commonly benchmarked algorithms. With this in mind we evaluate the performance of the proposed energy and optimize each method with



Fig. 7. Visual comparison for the evaluated methods and corresponding error values. The result of our OVTV produces the most accurate result, only marginally beaten by BM3D in terms of color accuracy. Yet, the visual quality of OVTV is more clear and does not suffer from desaturated colors as in DVTV.



Fig. 8. Example result images from the evaluation dataset for standard deviation 60 of Gaussian noise. In this image the OPP₁¹ performs shows better performance than the non-convex counter-parts. (PSNR/SSIM/CIEDE).



Fig. 9. Example result images from the evaluation dataset for standard deviation 60 of noise. OPP_p² performs well in images with piece-wise affine regions as indicated by the high SSIM value, although with respect to color consistency OPP₁¹ shows better result. (PSNR/SSIM/CIEDE).

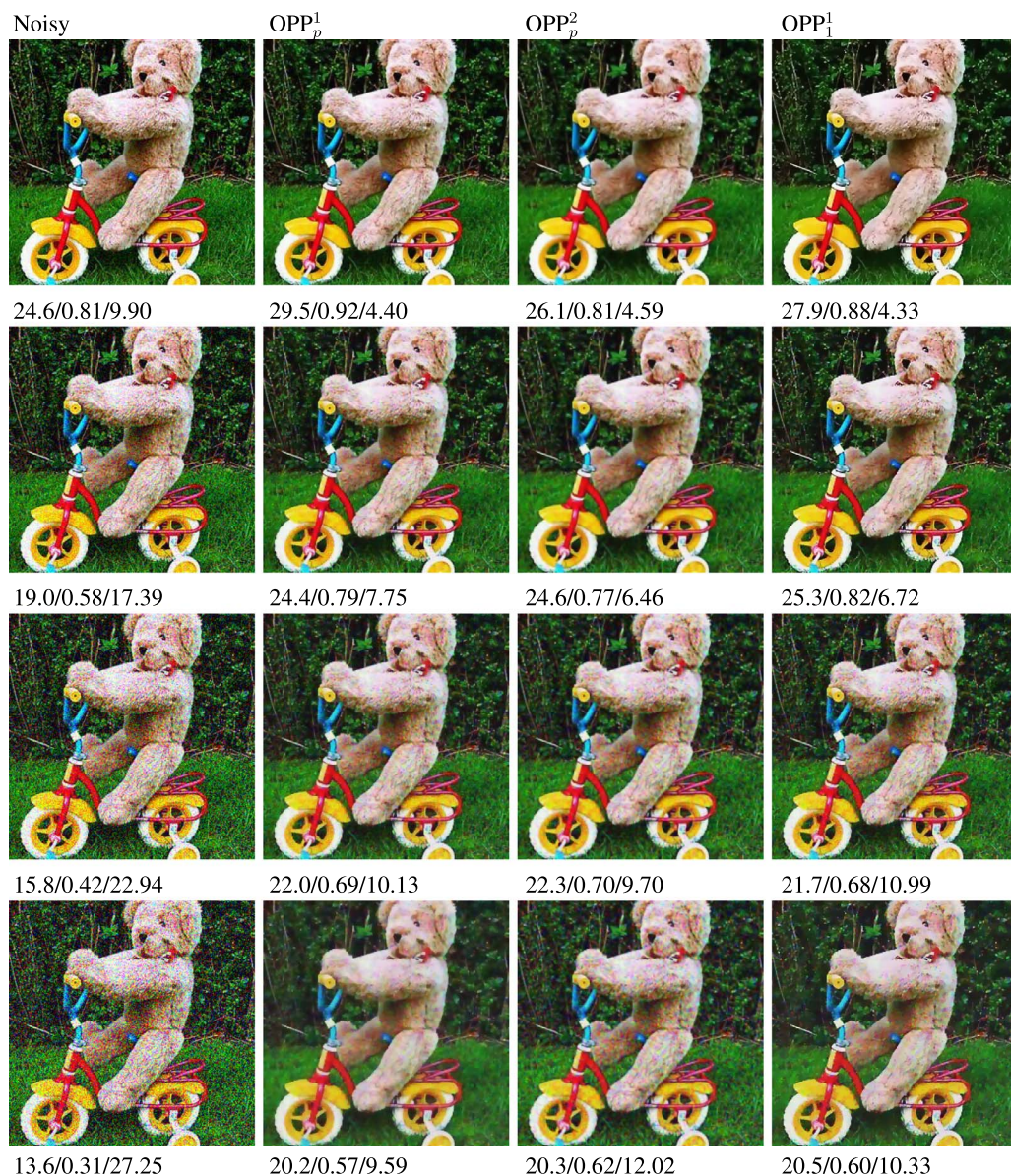


Fig. 10. Qualitative comparison between OPP. From top row to bottom row the noise levels the images are corrupted with noise of standard deviation 20, 40, 60 and 80. For higher noise-levels the second-order OPP_p^2 shows improved SSIM, in particular for noise level 80 shows less oversmoothing of the background image structure. Although, it contains more color shimmering reflected in the higher CIEDE value. For lower noise levels, the first-order methods seem preferable. (PSNR/SSIM/CIEDE).

Table 1

Error measures and standard deviation for the first and second-order OPP for varying p -values. These values were obtained in the optimization of the 100 images in the natural image denoising evaluation. Table 2 shows the best obtained results in this evaluation scenario.

PSNR/ p	OPP_p^1			OPP_p^2		
	0.3	0.6	0.9	0.3	0.6	0.9
20	32.4 ± 2.3	32.9 ± 2.0	33.0 ± 1.7	29.6 ± 3.4	30.0 ± 3.2	31.1 ± 2.7
40	27.5 ± 2.5	28.1 ± 2.4	28.4 ± 1.9	28.0 ± 2.4	28.0 ± 2.2	28.2 ± 1.9
60	24.5 ± 2.3	25.3 ± 2.0	25.5 ± 2.1	25.6 ± 1.9	25.6 ± 1.8	25.4 ± 1.9
80	22.7 ± 2.2	23.3 ± 2.1	23.4 ± 1.8	23.3 ± 1.9	23.3 ± 1.8	23.2 ± 1.9
SSIM						
20	0.90 ± 0.05	0.91 ± 0.05	0.91 ± 0.04	0.82 ± 0.09	0.84 ± 0.07	0.88 ± 0.05
40	0.79 ± 0.08	0.81 ± 0.08	0.83 ± 0.07	0.80 ± 0.08	0.81 ± 0.07	0.82 ± 0.06
60	0.69 ± 0.11	0.74 ± 0.09	0.75 ± 0.09	0.75 ± 0.08	0.75 ± 0.08	0.75 ± 0.08
80	0.63 ± 0.13	0.68 ± 0.11	0.69 ± 0.09	0.68 ± 0.10	0.69 ± 0.09	0.69 ± 0.09
CIEDE						
20	2.99 ± 2.64	2.97 ± 2.63	3.04 ± 2.64	3.42 ± 2.66	3.34 ± 2.63	3.23 ± 2.62
40	4.51 ± 2.54	4.40 ± 2.53	4.46 ± 2.55	4.61 ± 2.51	4.69 ± 2.52	4.73 ± 2.55
60	5.84 ± 2.48	5.64 ± 2.42	5.68 ± 2.42	5.86 ± 2.41	5.93 ± 2.43	5.95 ± 2.44
80	6.90 ± 2.31	6.81 ± 2.28	6.91 ± 2.28	7.09 ± 2.30	7.13 ± 2.31	7.14 ± 2.32

Table 2

Error measures for the evaluated methods for chromaticity noise. The best values are marked in bold. Although BM3D shows good color consistency, the proposed regularization strategy outperforms all competing variational methods w.r.t. structural and color consistency.

$\sigma = 20$	OPP_p^1	OPP_p^2	OPP_p^1	PDVTV (Bresson and Chan, 2008)	DVTV (Ono and Yamada, 2014)	TGV (Bredies et al., 2010)	BM3D (Dabov et al., 2007)	BM3DS (Dabov et al., 2007)
PSNR	32.9 ± 1.88	30.6 ± 2.84	32.0 ± 2.10	29.8 ± 2.04	27.0 ± 0.99	27.3 ± 2.74	32.9 ± 2.00	32.6 ± 1.19
SSIM	0.91 ± 0.04	0.86 ± 0.06	0.89 ± 0.05	0.85 ± 0.05	0.79 ± 0.08	0.78 ± 0.08	0.90 ± 0.05	0.87 ± 0.05
CIEDE	3.42 ± 2.71	3.11 ± 2.68	2.86 ± 2.68	4.75 ± 2.91	4.57 ± 2.48	5.44 ± 4.15	2.78 ± 2.66	3.63 ± 2.64
$\sigma = 40$								
PSNR	28.2 ± 2.14	28.4 ± 2.24	28.4 ± 1.93	25.9 ± 2.16	22.8 ± 2.17	25.4 ± 2.58	28.0 ± 2.61	27.5 ± 1.75
SSIM	0.81 ± 0.07	0.82 ± 0.07	0.82 ± 0.07	0.73 ± 0.08	0.60 ± 0.14	0.71 ± 0.09	0.79 ± 0.09	0.74 ± 0.07
CIEDE	4.88 ± 2.71	4.82 ± 2.58	5.16 ± 2.83	6.78 ± 3.06	7.12 ± 2.50	6.68 ± 3.60	4.31 ± 2.57	5.61 ± 2.60
$\sigma = 60$								
PSNR	25.2 ± 2.23	25.7 ± 2.05	25.9 ± 1.84	23.5 ± 1.66	21.9 ± 2.21	23.6 ± 2.05	25.2 ± 2.58	25.1 ± 2.07
SSIM	0.73 ± 0.10	0.76 ± 0.08	0.76 ± 0.09	0.60 ± 0.05	0.57 ± 0.16	0.65 ± 0.10	0.71 ± 0.12	0.68 ± 0.09
CIEDE	6.45 ± 3.28	6.56 ± 2.82	6.06 ± 2.57	9.22 ± 2.76	7.73 ± 2.52	8.21 ± 3.17	5.32 ± 2.46	6.23 ± 2.46
$\sigma = 80$								
PSNR	23.2 ± 1.97	23.4 ± 1.98	23.5 ± 1.82	20.9 ± 1.01	21.0 ± 2.04	21.9 ± 2.00	23.2 ± 2.37	23.2 ± 2.11
SSIM	0.68 ± 0.11	0.70 ± 0.10	0.70 ± 0.09	0.45 ± 0.06	0.55 ± 0.16	0.60 ± 0.11	0.66 ± 0.14	0.64 ± 0.12
CIEDE	7.22 ± 2.76	8.02 ± 2.95	7.92 ± 2.78	12.75 ± 2.40	8.31 ± 2.39	9.58 ± 3.46	6.39 ± 2.34	7.01 ± 2.29

Table 3

Error measures for the evaluated methods when the image's intensity and chromaticity components are corrupted by Gaussian noise. The values marked in bold show the best performing algorithm. BM3D shows the highest performance in each error measure and noise level, however considering the other competing variational methods our framework shows highly competitive results.

$\sigma = 20$	OPP_p^1	OPP_p^2	OPP_p^1	PDVTV (Bresson and Chan, 2008)	DVTV (Ono and Yamada, 2014)	TGV (Bredies et al., 2010)	BM3D (Dabov et al., 2007)	BM3DS (Dabov et al., 2007)
PSNR	30.6 ± 2.05	30.3 ± 2.55	30.4 ± 1.97	28.9 ± 2.34	30.4 ± 2.00	27.0 ± 3.11	32.2 ± 2.36	30.9 ± 1.86
SSIM	0.88 ± 0.03	0.86 ± 0.04	0.88 ± 0.03	0.83 ± 0.04	0.88 ± 0.03	0.77 ± 0.08	0.91 ± 0.03	0.86 ± 0.03
CIEDE	3.19 ± 2.68	3.18 ± 2.67	3.18 ± 2.67	4.57 ± 2.95	3.18 ± 2.68	5.00 ± 3.78	2.78 ± 2.70	3.88 ± 2.63
$\sigma = 40$								
PSNR	26.9 ± 2.33	27.4 ± 2.25	27.1 ± 2.35	25.6 ± 2.36	27.0 ± 2.02	25.1 ± 2.43	28.2 ± 2.48	26.5 ± 1.67
SSIM	0.77 ± 0.07	0.79 ± 0.06	0.78 ± 0.07	0.69 ± 0.07	0.78 ± 0.06	0.70 ± 0.09	0.81 ± 0.06	0.69 ± 0.05
CIEDE	4.44 ± 2.73	4.57 ± 2.73	4.56 ± 2.65	6.78 ± 3.04	4.35 ± 2.61	6.45 ± 3.06	4.32 ± 2.65	6.39 ± 2.56
$\sigma = 60$								
PSNR	25.0 ± 2.41	25.5 ± 2.33	25.2 ± 2.15	21.8 ± 0.93	25.0 ± 1.85	23.6 ± 2.50	26.7 ± 2.71	25.2 ± 1.84
SSIM	0.70 ± 0.09	0.72 ± 0.08	0.69 ± 0.06	0.44 ± 0.07	0.71 ± 0.08	0.63 ± 0.10	0.75 ± 0.08	0.63 ± 0.04
CIEDE	5.37 ± 2.77	5.46 ± 2.76	5.77 ± 2.64	11.25 ± 2.58	5.33 ± 2.53	7.78 ± 3.43	4.65 ± 2.68	7.09 ± 2.56
$\sigma = 80$								
PSNR	23.9 ± 2.25	24.2 ± 2.31	22.5 ± 1.21	17.3 ± 0.32	23.5 ± 1.76	22.6 ± 2.32	25.4 ± 2.67	23.7 ± 1.71
SSIM	0.65 ± 0.10	0.67 ± 0.10	0.50 ± 0.05	0.26 ± 0.08	0.65 ± 0.10	0.56 ± 0.10	0.70 ± 0.10	0.53 ± 0.04
CIEDE	5.86 ± 2.77	6.24 ± 2.90	8.14 ± 2.47	16.95 ± 2.30	6.19 ± 2.49	9.21 ± 3.38	5.35 ± 2.69	8.54 ± 2.56

respect to its parameters and noise levels. The following methods and parameter ranges are included in the evaluation and we refer to the respective works for further details:

- Decorrelated VTV (Ono and Yamada, 2014) (DVTV): Search space for optimal parameter configuration is $\tau \in \{0.95, 1, 1.05\}$, $w \in \{0.3, 0.4, 0.5, 0.6, 0.7\}$.
- Primal-dual VTV (Bresson and Chan, 2008) (PDVTV): The regularization parameter was optimized for 5 uniformly sampled values in the range 10^{-3} –0.2.
- Total generalized variation (Bredies et al., 2010) (TGV): Applied component-wise and only included for comparison. The regularization parameter was uniformly sampled with 5 values in the range 10^{-3} and 0.25.
- Color BM3D (Dabov et al., 2007) (BM3D): The standard deviation of the additive Gaussian noise was given as input.

We evaluate our double-opponent (OPP) formulation, see (23) for the case of a first (OPP_p^1) and second order energy OPP_p^2 . We restrict $q = p$ and let $p \in \{0.3, 0.6, 0.9\}$. The following parameter setup was

used:

- (OPP_p^1): First-order scheme optimized with $\mu \in \{10, 20, 30, 40, 80, 100\}$ and fixed $\alpha_1 = \beta_1 = 2$.
- (OPP_p^2): Second-order scheme optimized with $\mu \in \{10, 20, 30, 40, 80, 100\}$ and $\alpha_1 = \beta_1 = 2$ and $\alpha_2 = \beta_2 = 1$.
- (OPP_p^1): Optimized parameter space of μ are 5 uniformly sampled values from $1/255$ to $30/255$, $\alpha = 1$ and β was uniformly sampled in from 5 values in the range $1/255$ to $5/255$.

The experimental evaluation use 100 color images from the MSRA Salient Object Database (Liu et al., 2011). The image data were normalized to the range $[0, 1]$ from a 8-bit representation.

We are interested in consistent *color* image processing, that is we are specifically tackling the color image filtering problem. Accordingly, in addition to corrupting all image components by noise, we also consider the case that the *color* of the image is corrupted by additive Gaussian noise, not the intensity channel. Until now this denoising setup has not been benchmarked and poses an interesting task, i.e., the recovery of *color* information. Rather than corrupting *all* image data with additive

noise, we corrupt the components (o_2 and o_3) with standard deviations 20, 40, 60 or 80 of Gaussian noise and ignore the intensity channel. This color recovery scenario is of interest in, e.g., low-light conditions which can significantly reduce the image quality output of digital cameras (Bovik, 2005, Ch. 4.5) or in connection to typical JPEG compression where artifacts are frequently introduced due to different treatment of intensity and chrominance (Sharma, 2002, Ch. 8.6).

After transforming from the (now noisy) opponent representation to the RGB space, one can show that the r,g,b components retain a Gaussian noise distribution as the following calculation illustrates. Let σ_i^2 , $i = 1, 2, 3$ denote the standard deviation of zero mean Gaussian noise, then the opponent components, now seen as random variables, are normally distributed, i.e., $o_i \sim \mathcal{N}(0, \sigma_i^2)$. Transformation from the double-opponent space to the RGB color space is done via

$$u = O^{-1}o, \quad O^{-1} = \begin{pmatrix} 1/\sqrt{3} & 1/\sqrt{6} & 1/\sqrt{2} \\ 1/\sqrt{3} & 1/\sqrt{6} & -1/\sqrt{2} \\ 1/\sqrt{3} & -2/\sqrt{6} & 0 \end{pmatrix}. \quad (60)$$

Assuming normally distributed opponent components $o \sim \mathcal{N}(0, \Sigma_o)$, $\Sigma_o = \text{Diag}(0, \sigma^2, \sigma^2)$, we obtain $u \sim \mathcal{N}(0, \Sigma_u)$ with

$$\Sigma_u = O^{-1}\Sigma_o O^{-T}. \quad (61)$$

Excluding the inter-channel correlation between the r,g,b components in (61) the noise transformation is given by

$$u \sim \mathcal{N}\left(0, \frac{2}{3}\text{Diag}(\sigma^2, \sigma^2, \sigma^2)\right). \quad (62)$$

Therefore, we also evaluate BM3D with a scaled standard deviation. We denote this approach as

- Scaled-BM3D (BM3DS): Color BM3D with $\sqrt{2/3}$ of the noise standard deviation.

Next we present and discuss the results obtained with OPP and the compared methods. We present the color component denoising scenario first followed by the results for denoising all image components.

7.2.1. Results, chromaticity noise.

Table 2 shows the average PSNR, SSIM and CIEDE error measures for each method and noise level. Three methods stand out: OPP_p^1 , OPP_1^1 and BM3D. For lower noise-levels the non-convex first-order method OPP_p^1 shows highest PSNR and SSIM values. While OPP_1^1 performs marginally better than OPP_p^1 for noise levels larger than standard deviation 60 of noise, BM3D has the best CIEDE accuracy for all noise levels. Comparing only energy based methods (i.e., not BM3D/BM3DS) it is clear that all OPP-based methods show improved accuracy for PSNR, SSIM and CIEDE in all cases. In all cases OPP_p^2 shows worse accuracy than OPP_p^1 (except SSIM at noise level 60) due to the extra smoothness constraints imposed by the higher-order derivative. OPP_p^2 is more suitable for images with piecewise affine regions, such as illustrated in the synthetic example, Section 7.1.

The principal difference between OPP_1^1 and PDVTV is that the additional color mixing regularization term is included in the former, thus illustrating the success of the mixing term in OPP. With respect to error measures we see an improvement in each case for OPP_1^1 . Comparing the second order OPP_p^2 with the result of TGV the error value differences are smaller, however OPP still shows improved results.

The visual quality, comparing all methods for the (high) noise level 60, is seen in Fig. 7. All methods suffer from color shimmering in homogeneous regions, although, the shimmering is less obvious for BM3D, which also shows the best color consistency. Although, the

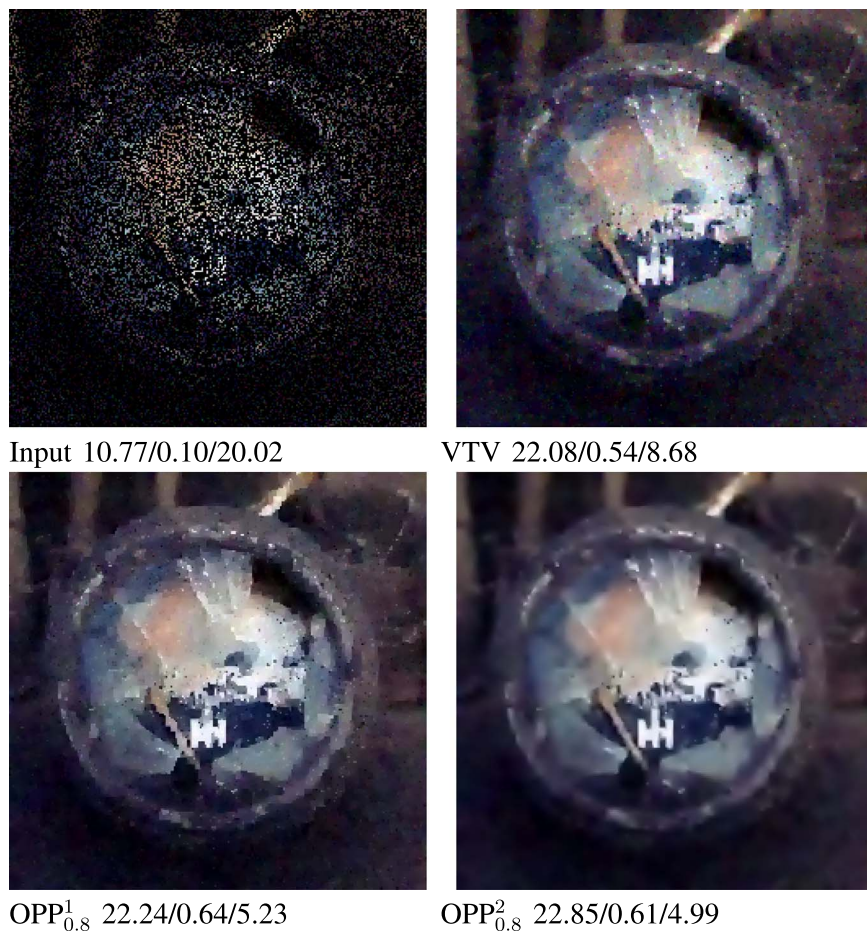


Fig. 11. The inpainting task is to restore the missing data samples in the upper left input image. Final results for vectorial formulations are seen on the second row for $p = 0.8$. All approaches produces convincing results without introducing disturbing color artifacts or oversmoothing.

result of BM3D is heavily oversmoothed, seen in the detailed panel and the trees in the background. All versions of the proposed OPP show higher PSNR and SSIM, although in these examples, there is color shimmering. DDTV shows the worst performance and shows strong structural oversmoothing of the trees in the background and there is strong evidence of color smearing. We remark that DDTV is designed for the color transform used in this work, however the method is fundamentally different from ours: DDTV considers the intensity and the color information as orthogonal and independent, and also regularize these separately, however, for the color image data, this is not the case in practice and the method fails as this assumption is violated.

Fig. 10 shows the output for the OPP methods for different noise levels. At the lowest noise-level the result images appear crisp and do not contain disturbing color artifacts at color edges. Color shimmering artifacts are naturally more pronounced as the noise level increases, due to imprecise parameter settings. Hand-tuning regularization parameters to separate image structure from noise increase clarity and suppress color shimmering, however, accurate determination of these parameters is subject to further study.

To additionally illustrate the recovery of noisy images using OPP, Figs. 8 and 9 show two challenging restoration scenarios where the images have been corrupted with standard deviation 60 of Gaussian noise. Fig. 8 is an image with vivid colors and many details, visually each methods performs well. OPP_1^1 appear most crisp and produces the most smooth background whereas $OPP_p^{1,2}$ both preserve the flower well. Fig. 9 shows similar characteristics as the previous example, although in this case OPP_p^2 shows a larger degree of color shimmering than OPP_p^1 and OPP_1^1 . Each methods do compensate for the image noise well and preserves facial-features and the stamp's text.

Table 1 shows the average error for the used p -values in the evaluation of the 100 natural images. There is an indication towards better

performance for PSNR and SSIM for p in the range 0.6–0.9 whereas CIEDE suggests smaller p -values for the first order scheme. Error values for the second order scheme is in general worse than the first order, this is due to the additional smoothness introduced by the higher-order derivatives. However, as seen in the synthetic result in Section 7.1, the second-order scheme performs very well when the image data is mostly affine.

7.2.2. Results, intensity and chromaticity noise.

It is also interesting to evaluate the proposed methods for the noise scenario when corrupting *all* image components with uniform noise. Table 3 shows the result for this scenario and it is clear that BM3D outperforms all compared methods in this general denoising task. However, comparing the proposed approach to the (more) similar variational methods PDVTV, DDTV and TGV our framework shows highly competitive results across all error measures and noise levels, illustrating the method as a viable alternative to existing methods for variational-based color image processing.

7.3. Image inpainting, image deblurring

Inpainting refers to the task of restoring *missing* image data. Fig. 11 illustrates the result for the non-convex OPP for the task of inpainting. This is a supervised inpainting task, consequently we define the operator K in our objective function to describe the region of interested to be inpainted, i.e., the missing data samples. Both versions of OPP perform well visually and quantitatively compared to VTV where we eliminated the influence of the color penalty term (47).

The second example is the task of restoring image data which has been corrupted by motion blur – a common problem in hand-held imaging devices. In this non-blind deblurring problem we restore the



Fig. 12. Example of image sharpening with known motion blur. This example shows that both our first and second order VTV formulations produce high-quality results without introducing disturbing color artifacts, oversmoothing homogeneous regions or over sharpening artifacts. (PSNR/SSIM/CIEDE).

input image, blurred with a motion kernel of 9 pixel shift at and angle of 10° counter-clockwise. The final restoration results for the different methods is seen in Fig. 12. Qualitatively all approaches compensate for the blur and produce similar results in this example image, however the first order scheme $\text{OPP}_{0.8}^1$ shows better error values. Eliminating the color term, as in the previous inpainting example, the result looks visually similar, however, $\text{OPP}_{0.8}^1$ shows improved error metrics, whereas $\text{OPP}_{0.8}^0$ shows worse PSNR but retains the color better than VTV.

8. Discussion and conclusion

We have shown that the double-opponent theory can significantly improve the performance of vectorial total variation-based methods. Motivated by recent and classical results in color theory, we let the inverse mapping from the opponent-space to the data space serve as a basis of our vectorial formulation. We showed that the inverse mapping encodes image colorfulness. We believe that as the field of perceptual psychophysics continue to evolve we will see further advances in color adaptive algorithms which are inspired by biology. The study presented in this work is a first step towards such models. We formulated a general energy that can model arbitrary higher-order derivatives, where all involved regularization terms can be convex, non-convex or a mixture. Automatic parameter selection for optimal restoration performance remains an open problem. We discretized and decomposed our formulation using the iterative Split Bregman scheme, and we demonstrated competitive performance compared to standard vectorial total variation methods and state of the art denoising algorithms evaluated using commonly used error measures in the image restoration community.

Acknowledgment

Support by the German Research Foundation (DFG) is gratefully acknowledged, grant GRK 1653.

References

- Åström, F., 2016. Color image regularization via channel mixing and half quadratic minimization. *ICIP*. pp. 4007–4011. <http://dx.doi.org/10.1109/ICIP.2016.7533112>.
- Åström, F., Baravdish, G., Felsberg, M., 2012. On tensor-based PDEs and their corresponding variational formulations with application to color image denoising. *ECCV*. LNCS 7574.
- Åström, F., Petra, S., Schmitzer, B., Schnörr, C., 2017. Image labeling by assignment. *J. Math. Imag. Vision* 1–28.
- Åström, F., Schnörr, C., 2016. Double-opponent vectorial total variation. *ECCV*. pp. 644–659.
- Attouch, H., Buttazzo, G., Michaille, G., 2014. *Variational Analysis in Sofolev and BV Spaces: Applications to PDEs and Optimization*, 2nd. SIAM.
- Ballester, C., Bertalmio, M., Caselles, V., Sapiro, G., Verdera, J., 2001. Filling-in by joint interpolation of vector fields and gray levels. *IEEE Trans. Image Process.* 10 (8), 1200–1211. <http://dx.doi.org/10.1109/83.935036>.
- Bergmann, R., Weinmann, A., 2016. A second-order tv-type approach for inpainting and denoising higher dimensional combined cyclic and vector space data. *J. Math. Imaging Vis.* 55 (3), 401–427.
- Bigun, J., Granlund, G.H., 1987. Optimal orientation detection of linear symmetry. *CVPR*. pp. 433–438.
- Blomgren, P., Chan, T., 1998. Color TV: total variation methods for restoration of vector-valued images. *IEEE Trans. Image Process.* 7 (3), 304–309.
- Bovik, A.C., 2005. *Handbook of Image and Video Processing (Communications, Networking and Multimedia)*. Academic Press, Inc., Orlando, FL, USA.
- Bredies, K., Kunisch, K., Pock, T., 2010. Total generalized variation. *SIAM J. Imag. Sci.* 3 (3), 492–526.
- Bresson, X., Chan, T., 2008. Fast dual minimization of the vectorial total variation norm and applications to color image processing. *Inverse Prob.* 24 (4), 455–484.
- Canny, J., 1986. A computational approach to edge detection. *IEEE Trans. Pattern Anal. Mach. Intell.* PAMI-8 (6), 679–698. <http://dx.doi.org/10.1109/TPAMI.1986.4767851>.
- Chambolle, A., 1994. Partial differential equations and image processing. *ICIP*. 1. pp. 16–20.
- Chambolle, A., 2004. An algorithm for total variation minimization and applications. *J. Math. Imag. Vision* 20 (1–2), 89–97. <http://dx.doi.org/10.1023/B:JMIV.0000011325.36760.1e>.
- Chambolle, A., Pock, T., 2011. A first-order primal-dual algorithm for convex problems with applications to imaging. *J. Math. Imag. Vision* 40 (1), 120–145.
- Chan, R.H., Liang, H.-X., 2014. Half-Quadratic Algorithm for ℓ_p - ℓ_q Problems with Applications to TV- ℓ_1 Image Restoration and Compressive Sensing. In: Bruhn, A., Pock, T., Tai, X.-C. (Eds.), *Efficient Algorithms for Global Optimization Methods in Computer Vision*. LNCS 8293. Springer, Berlin Heidelberg, pp. 78–103.
- Chan, T., Wong, C.-K., 1998. Total variation blind deconvolution. *IEEE Trans. Image Process.* 7 (3), 370–375. <http://dx.doi.org/10.1109/83.661187>.
- Chan, T.F., Golub, G.H., Mulet, P., 1999. A nonlinear primal-dual method for total variation-based image restoration. *SIAM J. Sci. Comp.* 20 (6), 1964–1977.
- Chan, T.F., Kang, S.H., Kang, Shen, J., 2002. Euler's elastica and curvature based inpaintings. *SIAM J. Appl. Math.* 63, 564–592.
- Chan, T.F., Kang, S.H., Shen, J., 2001. Total variation denoising and enhancement of color images based on the CB and HSV color models. *J. Vis. Commun. Image Represent.* 12 (4), 422–435.
- Chan, T.F., Mulet, P., 1999. On the convergence of the lagged diffusivity fixed point method in total variation image restoration. *SIAM J. Num. Analysis* 36 (2), 354–367. *CIE*, 1987. *International Lighting Vocabulary*. 4 CIE Publ, Vienna.
- Cohen, L.D., 1996. Auxiliary variables and two-step iterative algorithms in computer vision problems. *J. Math. Imag. Vision* 6 (1), 59–83.
- Conway, B.R., Chatterjee, S., Field, G.D., Horwitz, G.D., Johnson, E.N., Koida, K., Mancuso, K., 2010. Advances in color science: from retina to behavior. *J. Neurosci.* 30 (45), 14955–14963.
- Dabov, K., Foi, A., Katkovnik, V., Egiazarian, K., 2007. Color image denoising via sparse 3D collaborative filtering with grouping constraint in luminance-chrominance space. *ICIP*. 1.
- Duran, J., Moeller, M., Sbert, C., Cremers, D., 2016. Collaborative total variation: a general framework for vectorial tv models. *SIAM J. Imag. Sci.* 9 (1), 116–151.
- Ebner, M., 2007. *Color Constancy*, 1st. Wiley Publishing.
- Esser, E., 2009. Applications of Lagrangian-based alternating direction methods and connections to Split Bregman. *UCLA*, Technical Report 09–31, Computational and Applied Mathematics.
- Felsberg, M., Öjäll, K., Lenz, R., 2015. Unbiased decoding of biologically motivated visual feature descriptors. *Front. Rob. AI* 2, 20.
- Fornasier, M., March, R., 2007. Restoration of color images by vector valued functions and variational calculus. *SIAM J. Appl. Math.* 68 (2), 437–460.
- Förstner, W., Gülch, E., 1987. A fast operator for detection and precise location of distinct points, corners and centres of circular features. *ISPRS Intercommission, Workshop, Interlaken*. pp. 149–155.
- Gao, S., Yang, K., Li, C., Li, Y., 2013. A color constancy model with double-opponency mechanisms. *ICCV*. pp. 929–936. <http://dx.doi.org/10.1109/ICCV.2013.119>.
- Geman, D., Yang, C., 1995. Nonlinear image recovery with half-quadratic regularization. *IEEE Trans. Image Process.* 4 (7), 932–946. <http://dx.doi.org/10.1109/83.392335>.
- Goldluecke, B., Cremers, D., 2010. An approach to vectorial total variation based on geometric measure theory. *CVPR*. pp. 327–333.
- Goldluecke, B., Strelakovsky, E., Cremers, D., 2012. The natural vectorial total variation which arises from geometric measure theory. *SIAM J. Imag. Sci.* 5 (2), 537–563. <http://dx.doi.org/10.1137/110823766>.
- Goldstein, T., Osher, S., 2009. The Split Bregman method for l1-regularized problems. *SIAM J. Imag. Sci.* 2 (2), 323–343.
- Horn, B.K.P., Schunck, B.G., 1981. Determining optical flow. *Artif. Intell.* 17, 185–203.
- Hurlbert, A., Poggio, T., 1998. Synthesizing a color algorithm from examples. *Science* 239, 182–485.
- Iijima, T., 1959. Basic theory of pattern observation. *Papers of Technical Group on Automata and Automatic Control*, IECE, Japan.
- Joblove, G.H., Greenberg, D., 1978. Color spaces for computer graphics. *Proceedings of the 5th Annual Conference on Computer Graphics and Interactive Techniques*. ACM, pp. 20–25.
- Just, J., 2005. *Riemannian Geometry and Geometric Analysis*, 4th. Springer.
- Kappes, J., Andres, B., Hamprecht, F., Schnörr, C., Nowozin, S., Batra, D., Kim, S., Kausler, B., Kröger, T., Lellmann, J., Komodakis, N., Savchynskyy, B., Rother, C., 2015. A comparative study of modern inference techniques for structured discrete energy minimization problems. *Int. J. Comp. Vision* 115 (2), 155–184.
- Kass, M., Witkin, A., Terzopoulos, D., 1988. Snakes: active contour models. *Int. J. Comput. Vis.* 1 (4), 321–331.
- Kimmel, R., Malladi, R., Sochen, N., 2000. Images as embedded maps and minimal surfaces: movies, color, texture, and volumetric medical images. *Int. J. Comput. Vis.* 39 (2), 111–129.
- Koenderink, J.J., 1984. The structure of images. *Biol. Cybern.* 370 (50), 363–370.
- Land, E., 1983. Recent advances in retinex theory and some implications for cortical computations: color vision and the natural image. *Proc. Natl. Acad. Sci. USA* 80 (16), 5163–5169.
- Land, E., 1986. An alternative technique for the computation of the designator in the retinex theory of color vision. *Proc. Natl. Acad. Sci. USA* 83 (10), 3078–3080.
- Lenz, R., Latorre Carmona, P., 2010. Hierarchical s(3)-coding of RGB Histograms. In: Ranchordas, A., Pereira, J., AraEjo, H., Tavares, J. (Eds.), *Computer Vision, Imaging and Computer Graphics. Theory and Applications*. Communications in Computer and Information Science 68. Springer, Berlin Heidelberg, pp. 188–200.
- Liu, T., Yuan, Z., Sun, J., Wang, J., Zheng, N., Tang, X., Shum, H.Y., 2011. Learning to detect a salient object. *IEEE Trans. Pattern Anal. Mach. Intell.* 33 (2), 353–367.
- MacAdam, D.L., 1942. Visual sensitivities to color differences in daylight. *J. Opt. Soc. Am.* 32 (5), 247–273.
- Munsell, A., 1905. *A Color Notation*. G. H. Ellis Company.
- Newton, L., 1671. New theory about light and colors. *Philos. Trans.* 6 (69–80), 3075–3087.
- Oliveira, J.P., Bioucas-Dias, J.M., Figueiredo, M.A., 2009. Adaptive total variation image deblurring: a majorization-Minimization approach. *Signal Process.* 89 (9), 1683–1693.

- Ono, S., Yamada, I., 2014. Decorrelated vectorial total variation. *CVPR*. pp. 4090–4097.
- Perona, P., Malik, J., Pietro, P., 1990. Scale-space and edge detection using anisotropic diffusion. *IEEE Trans. Pattern Anal. Mach. Intell.* 12 (7), 629–639.
- Poynton, C., 2003. 24 - Luma and Color Differences. In: Poynton, C. (Ed.), *Digital Video and HDTV*. Morgan Kaufmann, San Francisco, pp. 281–300.
- Ratliff, F., 1971. Contour and contrast. *Proc. Am. Philos. Soc.* 115 (2), 150–163.
- Roth, S., Black, M.J., 2005. Fields of experts: a framework for learning image priors. *CVPR*. 2. pp. 860–867. <http://dx.doi.org/10.1109/CVPR.2005.160>.
- Rudin, L.I., 1987. *Images, Numerical Analysis of Singularities and Shock Filters*. California Institute of Technology Ph.D. thesis.
- Rudin, L.I., Osher, S., Fatemi, E., 1992. Nonlinear total variation based noise removal algorithms. *Phys. D* 60 (1–4), 259–268. [http://dx.doi.org/10.1016/0167-2789\(92\)90242-F](http://dx.doi.org/10.1016/0167-2789(92)90242-F).
- Sapiro, G., Ringach, D., 1996. Anisotropic diffusion of multivalued images with applications to color filtering. *IEEE Trans. Image Process.* 5 (11), 1582–1586. <http://dx.doi.org/10.1109/83.541429>.
- Sharma, G., 2002. *Digital Color Imaging Handbook*. CRC Press, Inc., Boca Raton, FL, USA.
- Sharma, G., Wu, W., Dalal, E.N., 2005. The CIEDE2000 color-difference formula: implementation notes, supplementary test data, and mathematical observations. *Color Res. Appl.* 30 (1), 21–30.
- Shevell, S.K., 2003. *The Science of Color*. Optical Society of America, 2003.
- sRGB, 2003. *Multimedia systems and equipment - colour measurement and management - part 2-1: colour management - default RGB colour space - sRGB*. IEC. 61966-2-1 (1999-10), ICS codes: 33.160.60, 37.080 - TC 100 - 51 pp. as amended by Amendment A1:2003.
- Tomasi, C., Manduchi, R., 1998. Bilateral filtering for gray and color images. *CVPR*. pp. 839–846. <http://dx.doi.org/10.1109/ICCV.1998.710815>.
- Tschumperlé, D., Deriche, R., 2003. Vector-valued image regularization with pde's: a common framework for different applications. *CVPR*. pp. 651–656.
- Wahlberg, B., Boyd, S., Annergren, M., Wang, Y., 2012. An admm algorithm for a class of total variation regularized estimation problems. *Preprints of the 16th IFAC Symposium on System Identification*. pp. 83–88.
- Wang, C., Komodakis, N., Paragios, N., 2013. Markov random field modeling, inference & learning in computer vision & image understanding: a survey. *Comput. Vision Image Understanding* 117 (11), 1610–1627.
- Wang, Z., Bovik, A., Sheikh, H., Simoncelli, E., 2004. Image quality assessment: from error visibility to structural similarity. *IEEE Trans. Image Process.* 13 (4), 600–612.
- Weickert, J., 1999. Coherence-enhancing diffusion filtering. *Int. J. Comput. Vis.* 31 (2–3), 111–127.
- Wu, C., Tai, X.-C., 2010. Augmented Lagrangian method, dual methods, and Split Bregman iteration for ROF, vectorial TV, and high order models. *SIAM J. Imag. Sci.* 3 (3), 300–339. <http://dx.doi.org/10.1137/090767558>.
- Zenko, S.D., 1986. A note on the gradient of a multi-image. *Comput. Vision Graph. Image Process.* 33 (1), 116–125.